Chaos in the model of repetitive phase transitions with hysteresis: Application to the self-sustained potential oscillations of lipid-bilayer membranes induced by gel–liquid-crystal phase transitions

Kouichi Yagisawa and Takeshi Kambara*
Department of Applied Physics and Chemistry, The University of Electro-Communications, Chofu, Tokyo 182, Japan

Masayoshi Naito
Advanced Research Laboratory, Hitachi Ltd., Hatoyama, Saitama 350-03, Japan
(Received 2 August 1993)

To clarify the mechanism of chaos generation and the routes to chaos in the self-sustained oscillation of the electric potential difference between two solutions divided by a lipid-bilayer membrane, a simple model of the system, the model of repetitive phase transitions with hysteresis, is presented in which oscillation is driven by repetitive gel–liquid-crystal phase transitions with hysteresis occurring in the lipid membrane and at the same time by a periodic external current. The dynamical property of the system is completely described by the nature of the function mapping the times at which the phase transition occurs successively. There exist various kinds of routes to chaos in the model of repetitive phase transitions with hysteresis (RPTH model) such as the period-doubling cascades, the intermittency, the quasiperiodic-chaotic transition, and the transition to chaos from complete phase locking. When the values of the system parameters satisfy certain conditions, the RPTH model becomes equivalent to the integrate-and-fire model and similar to the driven-relaxation-oscillator model. The model also generates structurally stable chaotic attractors which are never destroyed by a slight change in the values of system parameters. The attractors appear only for the regions of parameter values where the mapping function has at least one discontinuous point. This model contains the essential features of evolution behavior in various kinds of systems which generate iterative phase transitions with hysteresis.

PACS number(s): 64.70.Md, 05.45.+b, 87.10.+e, 87.22.Bt

I. INTRODUCTION

The excitable biomembranes exhibit a number of nonlinear phenomena important for living systems such as the generation and propagation of a nerve impulse, self-sustained oscillations of membrane potential in pacemaker neurons, and those of proton concentration on growing cell surfaces. Chaos in the electric potential oscillation has been demonstrated experimentally and theoretically in various types of excitable membrane systems. Especially a systematic investigation of chaos has been made in the electrically excitable systems driven by a periodic external current The experimental study has been made for cardiac cells [1], internodal cells of Nitella [2], pacemaker neurons of Onchidium [3–5], giant axons of squids [6–8], Purkinje fibers [9], and ventricular muscles [9]. The theoretical study also has been done for the Hodgkin-Huxley neural model [10,11], ventricular myocardial fibers [12], Purkinje fibers [13], and ganglion cells of Aplysia [14]. There have been also theoretical identifications of autonomous (nondriven) chaos in various kinds of membrane models such as bursting nerve cells [15,16], cardiac cells [13], pancreatic β cells [17], and a simple biophysically realistic model of an electrically excitable cell [18]. The oscillation phenomena mentioned above arise from the electric excitation of biomembranes which is driven by various types of voltage-gated ion channels.

There exists another type of membrane excitation, that is, the chemical excitation, in which the oscillations of flow and chemical potential difference of a transport species across membrane may occur with or without the electric potential oscillation [19,20]. These oscillations are driven by cooperative conformation changes of membrane transport proteins (allosteric proteins) whose activity is mostly independent of membrane potential [21,22]. Recently, we have shown, using a simple model of the chemically excitable membrane [23], that autonomous chaotic oscillations of ion concentrations around the membrane surface as well as those of membrane potential can be achieved by an appropriate coupling between two kinds of autocatalytic ion channels.

In the present paper we show theoretically that the lipid-bilayer membranes, including neither the voltage-gated ion channels nor the allosteric (autocatalytic) transport proteins, may produce the chaotic oscillations of the ion concentrations and of the membrane potential driven by a periodic external current. Recently, we presented a physically realistic model of the lipid-bilayer membrane in order to clarify the mechanism of self-sustained oscillation of the electric potential across the membrane [24]. The oscillation is driven by the repetitive gel–liquid-crystal phase transitions of the membrane in the model system. It was also shown there that an appropriate ap-

*To whom correspondence should be addressed.

plication of electric current across the membrane might induce the chaotic oscillation. The model, however, contains too many oscillating variables to analyze the features of the oscillations in detail. Therefore, we introduce here a simplified one-variable representation of the dynamics inherent in the previous model [24], in order to make clear the routes to chaos in the self-sustained oscillation of the electric potential between the two solutions divided by a lipid-bilayer membrane.

The simplified model describes the evolution of proton concentration on the membrane surface driven by both the repetitive gel–liquid-crystal phase transitions and a sinusoidal stimulating electric current. The transitions are generated by the repetitive adsorption and desorption of proton on the membrane surface which are induced by the periodic or a periodic reversal of the direction of protonic current. It is the essential condition for the reversal that the ion permeability across the membrane in the gel phase is noticeably different from that in the liquid-crystal phase and the phase transition has a hysteresis. The model is named "the model of repetitive phase transition with hysteresis" and is abbreviated hereafter to the RPTH model.

The time dependence of the proton concentration can be clearly understood by knowing when the iterative phase transitions occur, because the time dependence is represented analytically at the time between the successive phase transitions. Therefore, the dynamical property of the system is completely described by using the function mapping the times at which the phase transition occurs successively. The mapping function f is piecewise smooth and periodic with a period of unity as $f(\tau+1)=f(\tau)+1$. Since the function becomes smooth and monotonic for the sufficiently small amplitudes of the stimulating current, the proton concentration and the membrane potential vary with time periodically or quasiperiodically depending on the values of system parameters. The function becomes nonmonotonic for the sufficiently large amplitudes. Then the chaotic oscillation of proton concentration may appear and the quasiperiodic oscillation disappears. The phase locking of the oscillation may occur for quite wide ranges of the parameter values, that is, a complete phase locking may occur for an intermediate region of amplitude magnitude between the two extreme regions mentioned.

There exist various kinds of routes to chaos in the present model such as the periodic doubling cascades, the intermittency, and the quasiperiodic-chaotic transition. The model generates structurally stable chaotic attractors which are never destroyed by the slight change in the values of system parameters. The stable chaos has been observed only for the region of parameter values in which the mapping function has at least one discontinuous point. The RPTH model becomes equivalent to the integrate-and-fire model [25] when the values of the system parameters satisfy certain conditions. The dynamical property of the RPTH model becomes similar in some case to that of the modulated relaxation oscillator models [26–28]. The bifurcation scheme for the parameter dependence of dynamical property in the RPTH model contains the sequence "quasiperiodicity→complete phase locking→chaos," which has been found recently in the modulated-relaxation-oscillator models [27,28].

Although we have derived the RPTH model to analyze the chaos of self-sustained oscillations in the lipid-bilayer membrane system, the model contains the essential features of evolution behavior in various kinds of the systems which generate iterative phase transitions with a hysteresis. It is highly expected that the mechanism for chaotic behavior which we have found may be operative in those systems.

II. DESCRIPTION OF THE RPTH MODEL

A. Essential features of the previous model

Before describing the RPTH model, we explain briefly the previous model [24] for self-sustained potential oscillations of lipid-bilayer membranes induced by the gel–liquid-crystal phase transitions in order to make clear the physical meanings of the RPTH model. The system considered in the previous model consists of a lipid-bilayer membrane in aqueous solution which divides the solution into two regions. The bilayer consists of neutral and acidic lipid molecules. The ion species considered in the solution regions are proton H^+, hydroxide ion OH^-, a single kind of alkaline ion M^+, and a single kind of halogen ion A^-. There exist four kinds of regions with respect to the ion distribution in the system, which are the lipid-bilayer membrane, the diffuse electric double layers in the solution region produced by the membrane surface charges, the bulk solution regions, and the outermost solution regions as shown in Fig. 1. The ionic concentrations in the outermost solution regions are fixed and the bulk solutions are electrically neutral. The M^+ concentration C_M^{BR} in the right bulk solution is noticeably higher than that C_M^{BL} in the left bulk solution. The H^+ concentrations C_H^{BR} and C_H^{BL} in the right and left bulk solutions, respectively, are comparable to each other and substantially lower than C_M^{BL}. The anion concentrations in the double layers are extremely lower than those of cations, because the anions are repelled by the negative charges on the membrane surfaces. Each ionic concentration at the inside of the membrane surface is given by the product of the concentration of relevant ion at the outside of the membrane surface with the partition coefficient between the lipid membrane and the aqueous solution. Since the partition coefficient is much larger in the liquid-crystal state of the membrane than in the gel state, the ionic concentrations in the membrane are changed drastically by the gel–liquid-crystal phase transition.

The self-sustained oscillation of the electric potential difference ϕ_m across the membrane which is shown in Fig. 1 is induced by the repetitive phase transition of the lipid-bilayer membrane. We consider the case where the right half of the bilayer repeats the phase transition but the left half remains in the liquid-crystal state. The gel state of lipid layers in which the lipid molecules are close packed is generally stabilized with the H^+ adsorption on ionized polar heads of lipid molecules, while the desorp-

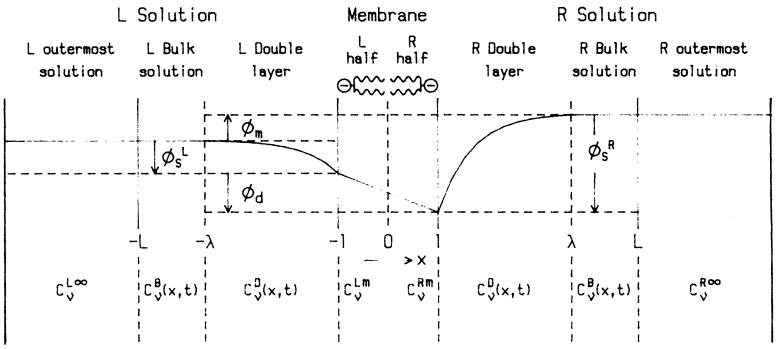

FIG. 1. Cross-section drawing of the system of a lipid-bilayer membrane dividing the solution into the three regions. Each solution consists of the outermost solution, the bulk solution, and the double-layer region. The electric potential ϕ and ion concentration C_ν are shown for each region.

tion of H^+ stabilizes the liquid-crystal state in which the molecules are loosely packed. Therefore, the state of each half of the bilayer depends on the concentration of H^+ in the diffuse electric double layer. Since the variations of the H^+ concentration is induced by the H^+ flux across the membrane, the change in the direction of the H^+ flux drives the phase transition. One cycle of the repetitive phase transition consists of the following processes. (i) H^+ ions flow into the right half being in the liquid-crystal state from the left solution. The direction of H^+ flux is determined by the flux of M^+ whose concentration in any region is overwhelmingly higher than the H^+ concentration. Since the anion concentrations in the membrane are negligibly small compared with the cation concentrations, the variation of cation distribution due to the M^+ flux Φ_{Mm} must be almost canceled out by that due to the H^+ flux Φ_{Hm}, that is, $\Phi_{Mm}+\Phi_{Hm}\doteq 0$. When both the lipid layers are in the liquid-crystal state, M^+ ions flow from the right solution to the left one because $C_M^R > C_M^L$. (ii) The ionized lipid molecules in the right half layer are neutralized by the H^+ ions flowing into the layer. (iii) When H^+ ions flow enough into the layer, the state of the layer is changed to the gel state. When the partition coefficient of M^+ between the right lipid layer and aqueous solution decreases more, largely due to the phase transition, than that of H^+, as assumed in the model, the direction of M^+ flux is reversed, because the M^+ flow from the right solution into the right lipid layer decreases drastically. (iv) The direction of the H^+ flux is also reversed due to the charge neutrality condition and the H^+ ions absorbed on the surface of the right lipid layer begin being desorbed. After enough H^+ is desorbed, the state of the layer returns to the initial liquid-crystal state.

Since there exists a hysteresis in the phase transition of the lipid layers, the surface concentration of H^+ at which the transition from the gel state to the liquid crystal state occurs is less by a definite amount than the concentration relevant to the reverse transition. This makes the time interval between the successive phase transitions finite. An appropriate application of alternating electric current across the membrane may induce the chaotic oscillations of the membrane potential.

B. Derivation of the RPTH model

We present the model which keeps the essence of the previous model but is reasonably simplified in order to investigate in detail the dynamical properties of self-sustained potential oscillations of lipid-bilayer membranes under application of alternating current. The key factor for the repetitive phase transitions is the H^+ concentration Y_H^R at the outside of the right lipid-layer surface as mentioned above. Because the ion concentrations in the double-layer regions are determined by those in the bulk solutions [24], we consider the time course only of the H^+ concentrations in the bulk solutions and assume that the M^+ concentrations in the solutions have no time dependence. The M^+ concentrations are several orders of magnitude larger than the relevant concentrations of H^+, while the change in the M^+ concentration is almost equal to that in the H^+ concentration, because the magnitude of the M^+ flux is almost equal to that of the H^+ flux. Therefore the relative change in the M^+ concentration is substantially less than that in the H^+ concentration. Furthermore, we are concerned only with the H^+ concentration averaged spatially over each bulk solution, because the spatial variation of the concentration is very small over the bulk solution region.

We derive the equations determining the time course of proton concentration in the solutions and the phase state of the right lipid layer. We define the quantity θ_X as

$$\theta_X \equiv \bar{C}_H^{BX} - \bar{C}_{OH}^{BX} - C_H^{X\infty} + C_{OH}^{X\infty} , \tag{2.1}$$

where the suffix X stands for the side L (left) or R (right), $\bar{C}_H^{BX}$ and $\bar{C}_{OH}^{BX}$ are the averaged concentrations of H^+ and OH^-, respectively, in the bulk solution on the side X, and $C_H^{X\infty}$ and $C_{OH}^{X\infty}$ are the fixed concentrations of H^+ and OH^-, respectively, in the outermost solution on the side X and are controllable parameter values. The variation rate of θ_X is given by

$$\frac{d\theta_X}{dt} = \frac{1}{w}(\Phi_{Hm}^X - \Phi_{HB}^X + \Phi_{OHB}^X) , \tag{2.2}$$

where w is the width of the bulk solution, Φ_{Hm}^X is the H^+ flux flowing from the X-side double layer to the X-side bulk solution, and Φ_{HB}^X and Φ_{OHB}^X are the fluxes of H^+ and OH^-, respectively, flowing from the X-side bulk solution to the outermost solution region (see Fig. 1). The fluxes are expressed by using θ_X as

$$-\Phi_{HB}^X + \Phi_{OHB}^X = -D\theta_X , \tag{2.3}$$

where D is an effective diffusion constant and is positive. Because the H^+ capacity of the alkylchain (hydrophobic)

region of the membrane is quite small, we can reasonably assume that

$$\Phi^L_{\mathrm{H}m}+\Phi^R_{\mathrm{H}m}=0 \ . \tag{2.4}$$

Then the relation

$$\theta_L+\theta_R=0 \tag{2.5}$$

is derived from Eqs. (2.1)–(2.4) for the initial condition that $\theta_L+\theta_R$ is zero. When an external electric current J is applied across the membrane, the relation

$$J=F(\Phi^R_{\mathrm{H}m}+\Phi^R_{Mm}) \tag{2.6}$$

arises from the continuity of the electric current, where Φ^R_{Mm} is the flux of M^+ flowing from the R double layer to the R bulk solution and F is the Faraday constant. It is briefly shown in Appendix A that the H^+ flux $\Phi^X_{\mathrm{H}m}$ in Eq. (2.2) is determined by θ_R and J through analytical functions including θ_R and J. The functions depend on the state of the membrane.

We consider the usual case where $|\theta_R|$ and J are very small compared with $C^{R\infty}_{\mathrm{H}}$ and $F|\Phi^R_{Mm}|$, respectively. Then $\Phi^X_{\mathrm{H}m}$ is reasonably approximated by a linear function of θ_R and J. Thus Eq. (2.2) is reduced to the simple form

$$\frac{d\theta_R}{dt}=\alpha_S+\beta_S\theta_R+\gamma_S J \ , \tag{2.7}$$

where α_S, β_S, and γ_S are the constant parameters determined by the properties of the system. The system parameters depend on the states of the right lipid layer through the partition coefficient κ^R_{H} between the lipid layer and the aqueous solution on the right side as shown in Appendix A. The state of the right lipid layer is determined by the charge density σ_R of the layer as shown in a previous paper [24]. Because σ_R depends monotonously on θ_R in the usual case as seen in Appendix A, the state is determined by the value of θ_R. We define the state index $S(t)$ at a time t as $S(t)=G$ for $\theta_R\geq\theta_{RG}$, $S(t)=L$ for $\theta\leq\theta_{RL}$, and $S(t)=S(t-\Delta t)$ for $\theta_{RL}<\theta_R<\theta_{RG}$, where G and L mean the gel and liquid-crystal states, respectively, and θ_{RG} and θ_{RL} are the threshold values of θ_R at which the state is changed from L to G and from G to L, respectively. Because the phase transition has a hysteresis, θ_{RG} is larger than θ_{RL}.

In order to investigate the effect of external electric current on the self-sustained oscillation of the membrane potential, it is enough that we know the dynamical properties of θ_R under the current application, because the membrane potential ϕ_m is determined by θ_R as shown in Appendix A. We use hereafter the normalized quantity Θ for θ_R for the convenience of clear understanding. The equations for Θ are written as

$$\frac{d\Theta}{d\tau}=\begin{cases}A_G+B_G\Theta+\Gamma_G\sin(2\pi\tau) & \text{for } S(\tau)=G\\ A_L+B_L\Theta+\Gamma_L\sin(2\pi\tau) & \text{for } S(\tau)=L\end{cases} \ , \tag{2.8}$$

and the state index $S(\tau)$ is given by

$$S(\tau)=\begin{cases}G & \text{for } \Theta(\tau)\geq 1\\ L & \text{for } \Theta(\tau)\leq -1\\ S(\tau-\Delta\tau) & \text{for } -1<\Theta(\tau)<1\end{cases} \ , \tag{2.9}$$

where

$$\Theta=2\frac{\theta_R-\theta_{RL}}{\theta_{RG}-\theta_{RL}}-1 \ , \tag{2.10}$$

$$J=J_0\sin(2\pi\nu t) \ , \tag{2.11}$$

$$\tau=\nu t \ , \tag{2.12}$$

$$A_S=\frac{2\alpha_S+(\theta_{RG}+\theta_{RL})\beta_S}{\nu(\theta_{RG}-\theta_{RL})} \quad (S=G,L) \ , \tag{2.13}$$

$$B_S=\frac{\beta_S}{\nu} \quad (S=G,L) \ , \tag{2.14}$$

$$\Gamma_S=\frac{2J_0\gamma_S}{\nu(\theta_{RG}-\theta_{RL})} \quad (S=G,L) \ . \tag{2.15}$$

Here, as shown in Eq. (2.11), we choose a sinusoidal electric current with frequency ν as the applied current J. The parameters A_S, B_S, and Γ_S correspond effectively to the proton flux, the diffusion coefficient of H^+ across the membrane, and the amplitude of external current, respectively, for the state S of the right lipid layer. The values of B_G and B_L are negative in the present system, that is, they mean the damping factors for the oscillation of Θ.

C. Mapping function of the transition times

Since Eq. (2.8) can be analytically solved as long as the state $S(\tau)$ does not change, the time dependence of Θ is clearly understood by knowing the times at which the iterative phase transitions occur. Therefore, we derive here the mapping function for the iterative transition times. Since the applied force is periodic, the mapping becomes a kind of circle map. By solving Eq. (2.8) for $S(\tau)=G$ and L, we obtain

$$\Theta(\tau)=\Theta_S(\tau;T_S)$$

$$\equiv\begin{cases}A_S(\tau-T_S)-G_S\cos(2\pi\tau) & \text{for } B_S=0\\ \dfrac{A_S}{B_S}\{\exp[B_S(\tau-T_S)]-1\}-G_S\cos(2\pi\tau+\delta_S) & \end{cases} \tag{2.16}$$

$$\text{for } B_S\neq 0 \ , \tag{2.17}$$

where the suffix S stands for the state G or L, T_S is the integration constant, and

$$G_S\equiv\Gamma_S(B_S^2+4\pi^2)^{-1/2} \ , \tag{2.18}$$

$$\delta_S\equiv\arctan\left[-\frac{B_S}{2\pi}\right] \ . \tag{2.19}$$

We denote the time of a phase transition from L (liquid-crystal state) to G (gel state) by τ_{LG} and that from G to L by τ_{GL}. The equations

$$\Theta_L(\tau_{GL};T_L)=-1 \ , \tag{2.20}$$

$$\Theta_G(\tau_{LG};T_G)=1 \tag{2.21}$$

are satisfied just after the phase transition. The integration constants T_L and T_G are obtained from Eqs. (2.20) and (2.21), respectively, as

$$T_S=H_S(\tau_{RS}) \equiv \begin{cases} \tau_{RS}-\dfrac{1}{A_S}\{G_S\cos(2\pi\tau_{RS})\mp 1\} & \text{for } B_S=0 \\ \tau_{RS}-\dfrac{1}{B_S}\ln\left[1+\dfrac{B_S}{A_S}\{G_S\cos(2\pi\tau_{RS}+\delta_S)\mp 1\}\right] & \text{for } B_S\neq 0\ , \end{cases} \tag{2.22, 2.23}$$

where S takes L or G, R takes G for $S=L$ and L for $S=G$, the upper sign is used for $S=L$, and the lower one is for $S=G$. We use hereafter the double signs with the same meaning.

We introduce the partial mapping functions $f_L(\tau_{GL})$ and $f_G(\tau_{LG})$, which transform τ_{GL} and τ_{LG}, respectively, to the subsequent transition time from L to G and that from G to L. A typical situation of time course of Θ is shown in Fig. 2(a). The transition time $f_S(\tau_{RS})$ subsequent to τ_{RS} is given by

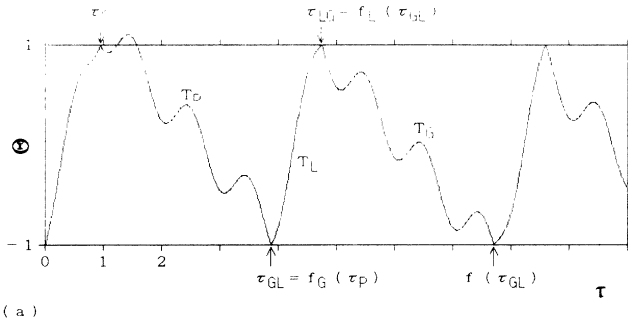

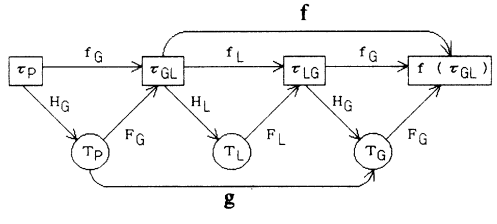

FIG. 2. (a) A typical time dependence of the concentration fluctuation Θ of H^+ and OH^- defined by Eq. (2.1). The phase transitions occur at the times indicated with arrows. The normalized concentration fluctuation Θ and the reduced time τ have no dimension. (b) Schematic explanation of the functions f_G, f_L, f, g, H_G, H_L, F_G, and F_L, and functional relations between the transition time τ_{RS} and the integration constant T_S in Eqs. (2.16) and (2.17).

$$f_S(\tau_{RS})=\min\{\tau;\Theta_S(\tau;H_S(\tau_{RS}))=\pm 1\ ;\ \tau>\tau_{RS}\}\ , \tag{2.24}$$

where $\min\{\tau;\Omega\}$ means the minimum value of τ fulfilling the condition Ω. The solutions τ of $\Theta_S(\tau;H_S(\tau_{RS}))=\pm 1$ correspond to the times when the transition from S to R occurs. We can obtain the transition time subsequent to τ_{RS} through the conditions of $\tau>\tau_{RS}$ and $\min\{\tau\}$.

Because we are concerned with the continuous oscillation of $\Theta(\tau)$, that is, with the iterative phase transitions, we consider the problem only for the ranges of the parameters A_S, B_S, and G_S in which Eq. (2.24) always has solutions. The ranges are

$$A_L>0 \text{ for } B_L=0\ ,\quad A_G<0 \text{ for } B_G=0\ ; \tag{2.25}$$

$$-\frac{A_L}{B_L}+|G_L|>1 \text{ for } B_L<0\ ,$$

$$\frac{A_G}{B_G}+|G_G|>1 \text{ for } B_G<0\ ; \tag{2.26}$$

$$-\frac{A_L}{B_L}+|G_L|<-1 \text{ for } B_L>0\ ,$$

$$\frac{A_G}{B_G}+|G_G|<-1 \text{ for } B_G>0\ . \tag{2.27}$$

These are the conditions that the values of $\Theta_S(\tau;T_S)$ can pass the threshold ($\Theta=1$ for $S=L$ and $\Theta=-1$ for $S=G$) with increasing τ.

We introduce the total mapping function $f(\tau_{GL})$, which transforms τ_{GL} to the time of the subsequent transition from G to L and is given by

$$f(\tau_{GL})\equiv f_G(f_L(\tau_{GL}))\ . \tag{2.28}$$

The total mapping consists of the alternative application of the partial mappings f_L and f_G. Since the right-hand side of Eq. (2.8) is periodic with respect to τ, the partial mapping functions f_S ($S=L,G$) are periodic as

$$f_S(\tau_{RS}+1)=f_S(\tau_{RS})+1\ . \tag{2.29}$$

Therefore, the total mapping function f is also periodic as

$$f(\tau_{GL}+1)=f(\tau_{GL})+1\ . \tag{2.30}$$

For the convenience of later calculation, we derive an alternative total mapping function g of the integration constant T_G, which is in many cases equivalent to f and much simpler. When $|G_S|$ is not too large (say $|G_S|<1$), the equation $\Theta_S(\tau;T_S)=\pm 1$ in the definition (2.24) of f_S has no solution for $\tau\leq\tau_{RS}$, that is, the subsidiary condition $\tau>\tau_{RS}$ in Eq. (2.24) is not necessary. Then the value of $f_S(\tau_{RS})$, τ_{SR}, is determined uniquely by the value of T_S so that we can represent τ_{SR} as the function of T_S, $F_S(T_S)$, where

$$\tau_{SR}=F_S(T_S)\equiv\min\{\tau;\Theta_S(\tau;T_S)=\pm 1\}\ . \tag{2.31}$$

In the case where B_S is negative, $F_S(T_S)$ increases or decreases monotonously with increasing T_S depending on

whether $\pm A_S \exp(-B_S T_S)$ is positive or negative, respectively. On the other hand, $F_S(T_S)$ increase monotonously in the case where B_S is positive. The correspondences between the sequence of transition times τ_{GL}, τ_{LG}, and $f(\tau_{GL})$ and the sequence of integration constants T_P, T_L, and T_G are shown in Figs. 2(a) and 2(b). Since τ_{GL} is determined uniquely by T_P, $T_G = H_G(f_L(\tau_{GL}))$ is also determined uniquely by T_P as seen in Fig. 2(b). The transformation from T_P to T_G is represented by using the mapping function $g(T)$ as $T_G = g(T_P)$, where

$$g(T_P) \equiv H_G(f_L(F_G(T_P))) . \tag{2.32}$$

Since $H_S(\tau_{RS}+1) = H_S(\tau_{RS})+1$ and $F_S(T_S+1) = F_S(T_S)+1$, using Eqs. (2.29) and (2.32) we obtain

$$g(T_P+1) = g(T_P)+1 . \tag{2.33}$$

The mapping given by $g(T_P)$ is also a circle map with mod1. The graphic representation of the mapping function g becomes simpler in many cases than that of f. However, the use of g gives invalid results for very large values of $|G_G|$ because $f_G(\tau_{LG})$ cannot be uniquely determined by T_G for those values. Then we must use f in order to investigate the dynamical properties of Θ.

III. DYNAMICAL PROPERTY OF THE MEMBRANE SYSTEM UNDER ALTERNATING CURRENT

A. The relation of characteristics of the mapping function with the dynamical property

The dynamical property of the membrane system under the application of sinusoidal electric current can be understood through the dynamical property of the fluctuation Θ of the H^+ concentration which is determined by Eq. (2.8). The time dependence of Θ can be described by the chronological sequence of the transition time τ_{GL}. Because the sequence is derived by the iterative operation of the mapping function f, we investigate here how the characteristic features of f depend on the values of system parameters A_S, B_S,and Γ_S ($S = L, G$).

First, we summarize the relations between the characteristic features of f and the dynamical property of the sequence of τ_{GL}. When the function f is monotonic, the rotation number ρ is defined uniquely. The sequence $\{f^n(\tau)\}$ is asymptotically periodic in modulus 1 in the case where ρ is rational, while it becomes quasiperiodic in the case where ρ is irrational. When f is monotonic and sufficiently smooth, the measure of quasiperodicity in the parameter space becomes positive. However, when f has one or more discontinuous points, the measure may become zero [29]. When f is nonmonotonic, the chaotic sequence may appear depending on the parameter values. Chaos may appear in the dynamical property when the monotonicity of f is lost by changing the parameter values, but the quasiperodicity is suppressed when either the monotonicity or the continuity of f is lost.

Second, we consider the dependence of the characteristic features of f on the values of system parameters. Since the function f consists of f_L and f_G as shown in Eq. (2.28), f becomes monotonic (continuous) only when both f_L and f_G are monotonic (continuous). The function f_L is monotonic if and only if $d\Theta_L/d\tau \geq 0$ for every τ at which $\Theta_L(\tau) = -1$. This condition is fulfilled in the parameter region

$$A_L - B_L - |\Gamma_L| \geq 0 , \tag{3.1}$$

as seen from Eq. (2.8). The reason why Eq. (3.1) becomes the necessary and sufficient condition for the monotonicity of f_L is as follows. It is seen from Eqs. (2.16) and (2.17) that the equation

$$\Theta_S(\tau;T_{S1}) - \Theta_S(\tau;T_{S2}) = \{\Theta_S(\tau_0;T_{S1}) - \Theta_S(\tau_0;T_{S2})\} \times \exp[B_S(\tau-\tau_0)] \tag{3.2}$$

holds for arbitrary values of τ, τ_0, and T_{S1}, and T_{S2}. We consider the two time courses $\Theta_L(\tau;H_L(\tau_A))$ and $\Theta_L(\tau;H_L(\tau_B))$, where τ_A and τ_B are the transition times and satisfy the equations $\Theta_L(\tau_A;H_L(\tau_A)) = -1$ and $\Theta_L(\tau_B;H_L(\tau_B)) = -1$, respectively. Because the condition $d\Theta_L(\tau;T_L)/d\tau \geq 0$ for $\Theta_L(\tau;T_L) = -1$ is satisfied for Eq. (3.1), the inequality $\Theta_L(\tau_B;H_L(\tau_A)) > \Theta_L(\tau_A;H_L(\tau_A))$ $[= \Theta_L(\tau_B;H_L(\tau_B))]$ holds for $\tau_B > \tau_A$. Using this and Eq. (3.2) we obtain the relation $\Theta_L(\tau;H_L(\tau_A)) > \Theta_L(\tau;H_L(\tau_B))$ for any τ. The next transition time $f_L(\tau_B)$ determined from $\Theta_L(\tau;H_L(\tau_B)) = 1$ becomes larger than $f_L(\tau_A)$ obtained from $\Theta_L(\tau;H_L(\tau_A)) = 1$. Therefore, the mapping function $f_L(\tau)$ increases monotonously with τ if Eq. (3.1) holds. On the other hand, if Eq. (3.1) fails, $d\Theta_L/d\tau$ becomes negative for some τ at which $\Theta_L(\tau) = -1$. Then, $f_L(\tau_B)$ may become smaller than $f_L(\tau_A)$ even for $\tau_B > \tau_A$, if $d\Theta_L/d\tau < 0$ for $\tau = \tau_A$ and τ_B.

The mapping function f_L is continuous if and only if $d\Theta_L/d\tau \geq 0$ for every τ at which $\Theta_L(\tau) = 1$. This condition is fulfilled in the parameter region

$$A_L + B_L - |\Gamma_L| \geq 0 , \tag{3.3}$$

as seen from Eq. (2.8). The function $f_L(\tau)$ becomes smooth everywhere for $A_L + B_L - |\Gamma_L| > 0$. When $d\Theta_L/d\tau \geq 0$ at the threshold line $\Theta = 1$, the curve of $\Theta = \Theta_L(\tau;H_L(\tau_A))$ crosses this line only once at $\tau = f_L(\tau_A)$. It is seen from Eqs. (2.16) and (2.22) or from Eqs. (2.17) and (2.23) that $\Theta_L(\tau;H_L(\tau_A))$ is a smooth function of τ_A. Therefore, it can be shown by the implicit function's theorem that $f_L(\tau_A)$ is a continuous function of τ_A. On the other hand, if Eq. (3.3) fails, there exists some region of τ where $d\Theta_L/d\tau$ becomes negative for τ at which $\Theta_L(\tau) = 1$. Then it can be seen that f_L has a discontinuous point τ_C and that $f_L(\tau)$ cannot take any value between $f_L(\tau_C - 0)$ and $f_L(\tau_C + 0)$. Therefore, Eq. (3.3) is the necessary and sufficient condition for the continuity of f_L.

From the similar consideration for the function f_G we obtain the necessary and sufficient condition for the monotonicity of f_G as

$$A_G + B_G + |\Gamma_G| \leq 0 \tag{3.4}$$

and the condition for the continuity of f_G as

$$A_G - B_G + |\Gamma_G| \leq 0 \ . \tag{3.5}$$

The function f_G becomes smooth everywhere for $A_G - B_G + |\Gamma_G| < 0$. Thus the mapping function f defined by Eq. (2.28) becomes monotonic in the parameter regions where Eqs. (3.1) and (3.4) are satisfied, and f is continuous in the regions where Eqs. (3.3) and (3.5) are satisfied.

We divide the parameter space into three regions as follows on the basis of the characteristic feature of f. The function f is monotonic and continuous in region I, monotonic and discontinuous in region II, and nonmonotonic in region III. The chronological sequence of the transition time τ_{GL} is quasiperiodic or asymptotically periodic in region I. It may be asymptotically periodic in almost all parts of region II and chaotic or asymptotically periodic in almost all parts of region III.

We can define similarly the three parameter regions also by using the feature of the alternative mapping function g given by Eq. (2.32). However, the regions based on g are not necessarily equivalent to the corresponding regions based on f even in the parameter region where the use of g is quite reasonable. For example, when f and g are discontinuous, it may happen in some region that g is monotonic but f is nonmonotonic. This occurs in the case where f is monotonic within the range of $f(\tau)$ but not monotonic over the whole range of τ. Although the parameter values corresponding to such cases are classified into region III by using f, they are classified into region II by using g and the chronological sequence of T_G obtained by using monotonic g is not chaotic. Thus the classification into region III through f does not necessarily mean that the solution is chaotic. The classification of parameter values through g gives a more detailed information about the dynamical property of the system than that through f does. However, the use of g becomes invalid for some region of the parameter values and the representation for the classification of parameter regions through g is much more complicated than that through f. Therefore, we adopt hereafter the classification of the parameter regions obtained through f, though we also use g in order to investigate the dynamical property of the system in detail.

B. Mechanisms of chaos generation

We have stated in Sec. III A that chaos may appear in region III ($A_L - B_L - |\Gamma_L| < 0$ or $A_G + B_G + |\Gamma_G| > 0$) of the parameter space where the mapping function f is nonmonotonic. On the basis of the analytical consideration and the numerical calculations, we describe the mechanisms of chaos generation and show in what parts of region III the chaotic sequences of τ_{GL} can be usually obtained. When we scan the parameter space for the purpose mentioned, it is difficult for us to change independently the six parameter values (A_S, B_S, Γ_S for $S = L, G$). These parameters consist of two kinds of quantities where one is inherent in the membrane systems and the other comes from the eternally applied current. In order to change the two kinds of quantities independently, we represent the six parameters as

$$A_S = \frac{A_{S0}}{\nu} \quad (S = L, G) \ , \tag{3.6}$$

$$B_S = \frac{B_{S0}}{\nu} \quad (S = L, G) \ , \tag{3.7}$$

$$\Gamma_S = \frac{\Gamma_{S0} J_0}{\nu} \quad (S = L, G) \ , \tag{3.8}$$

where A_{S0}, B_{S0}, and Γ_{S0} are the quantities inherent in the system and J_0 and ν are the amplitude and frequency of the current. In the present section, we sweep only two parameters at the same time, where one is chosen among A_{S0}, B_{S0}, and Γ_{S0} and the other is done among J_0 and ν.

1. *Phase shift*

In the parameter region where B_G and $B_L \leq 0$, chaos is generated mainly by the mechanism that is referred to as "the phase shift." In order to make our consideration easy, we fist treat the simple case of $B_G = B_L = 0$ and $\Gamma_L = 0$. The results for $B_G = B_L = 0$ are almost straightforwardly applicable for the cases of $B_G < 0$ and $B_L < 0$, unless $|B_G|$ and/or $|B_L|$ are not so large. Region III, where the chaotic sequence of τ_{LG} and τ_{Gl} may occur, is given by the condition $|\Gamma_G| > -A_G$. We can know the property of the mapping function g in the special case as follows. We take τ_0 as the initial value of τ_{LG} and obtain the sequence of τ_k ($k = 0, 1, 2$) by using f_G and f_L as $\tau_1 = f_G(\tau_0)$ and $\tau_2 = f_L(\tau_1)$. We define also T_k by $T_k = H_G(\tau_k)$ for $k = 0, 1, 2$, where they satisfy the relation $g(T_0) = T_2$. We derive here the relation between T_k and T_{k+1} for $k = 0$ and 1. Because the equations

$$\Theta_S(\tau; H_S(\tau)) = \mp 1 \ , \tag{3.9}$$

$$\Theta_S(f_S(\tau); H_S(\tau)) = \pm 1 \tag{3.10}$$

hold for every τ by the definitions of H_S and f_S, we obtain the relations $\Theta_G(\tau_1; H_G(\tau_1)) = 1$ and $\Theta_G(\tau_1; H_G(\tau_0)) = -1$ by substituting $\tau = \tau_1$ and τ_0 into Eqs. (3.9) and (3.10), respectively for $S = G$. Substituting Eq. (2.16) into these relations, we obtain

$$T_1 = T_0 - \frac{2}{A_G} \ . \tag{3.11}$$

We also substitute Eq. (2.16) into the relations $\Theta_L(\tau_R; H_L(\tau_1)) = 1$ and $\Theta_L(\tau_1; H_L(\tau_1)) = -1$, which are derived by substituting $\tau = \tau_1$ into Eqs. (3.10) and (3.9) for $S = L$. Then we obtain

$$\tau_2 = f_L(\tau_1) = \tau_1 + \frac{2}{A_L} \ . \tag{3.12}$$

By using $T_2 = H_G(\tau_2)$ and Eq. (3.12), T_2 is expressed in terms of T_1 as

$$T_2 = H_G\left[\tau_1 + \frac{2}{A_L}\right] = H_G\left[H_G^{-1}(T_1) + \frac{2}{A_L}\right] \ , \tag{3.13}$$

where $H_G^{-1}(T_1)$ means the inverse function of $H_G(\tau_1)$. Thus the mapping function $g(T_0)$ is denoted by

$$g(T_0)=T_2=H_G\left[H_G^{-1}\left[T_0-\frac{2}{A_G}\right]+\frac{2}{A_L}\right] . \quad (3.14)$$

We consider first the dependence of g on the values of A_L and A_G and secondly that of g on Γ_G. In the special case where $2/A_L$ is equal to an integer n, Eq. (3.14) is simplified as

$$g(T_0)=T_0+n-\frac{2}{A_G} , \quad (3.15)$$

by using the equation $H_G(\tau+n)=H_G(\tau)+n$, which is deduced from Eq. (2.22). The sequence of T generated by g is quasiperiodic when A_G is irrational, while it is periodic when A_G is rational. The periodic solutions are neutrally stable. In the case where $|\Gamma_G|>-A_G$ and $2/A_G$ deviates slightly from an integer n, some bifurcation takes place. By substituting $2/A_L=n+\mu$ ($|\mu|<1$) into Eqs. (3.13) and (3.14), we obtain

$$T_2=H_G(H_G^{-1}(T_1)+\mu)+n , \quad (3.16)$$

$$g(T)=H_G\left[H_G^{-1}\left[T-\frac{2}{A_G}\right]+\mu\right]+n . \quad (3.17)$$

We show graphically the alternative mapping function g given by Eq. (3.17) for $\mu=-0.1$ and 0.1 in Figs. 3(a) and 3(b), respectively. In the case where $\mu<0$ and $|\mu|\ll 1$, the inequality $g(T_D-0)>g(T_D+0)$ holds at the discontinuous point T_D and the derivative of g becomes positive everywhere as seen in Fig. 3(a). Then, the iterative operating of g usually generates chaos, as shown in Fig. 4, because the average of the derivative of g exceeds unity. On the other hand, when $\mu>0$ and $|\mu|\ll 1$, the absolute value of average of $dg(T)/dT$ becomes less than unity as seen in Fig. 3(b), because the inequality $g(T_D-0)<g(T_D+0)$ holds at T_D. Then it is rare for the system to generate chaos as shown in Fig. 4.

Now we consider the effect of Γ_G to the chaos generation in the case where $B_G=B_L=0$ and $\Gamma_L=0$. In the parameter region where $|\Gamma_G|\gg -A_G$ and the use of g is

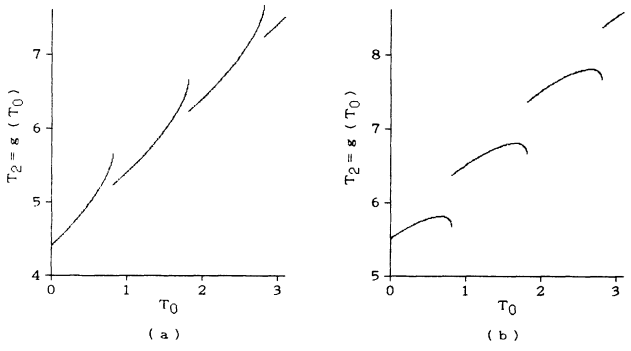

FIG. 3. Graphical representation of the mapping function g in the case of $A_G=-1$, $B_G=0$, and $\Gamma_G=5$: (a) $2/A_L=2+\mu$, where $\mu=-0.1$. The inequality $g(T_D-0)>g(T_D+0)$ holds at the discontinuous point T_D and the derivative of g is positive everywhere; (b) $2/A_L=2+\mu$, where $\mu=0.1$. The inequality $g(T_D-0)<g(T_D+0)$ holds and the average of the derivative of g is less than unity.

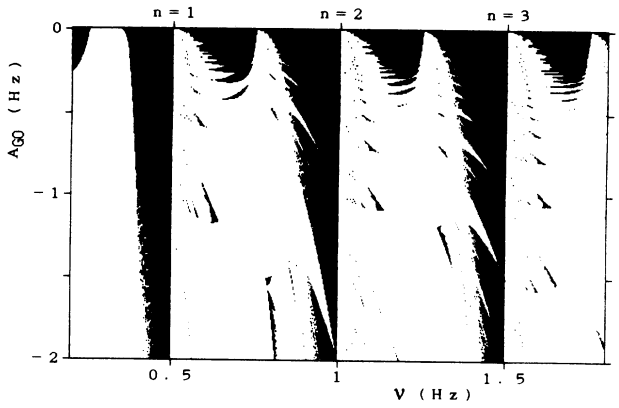

FIG. 4. Phase diagram for the dynamical property of the RPTH system in the case of $A_{L0}=1$ Hz, $B_{L0}=0$ Hz, $B_{G0}=0$ Hz, $\Gamma_{L0}=0$ Hz $A^{-1}m^2$, $\Gamma_{G0}=3\times10^4$ Hz $A^{-1}m^2$, and $J_0=1\times10^{-4}$ $A\,m^{-2}$ (see Ref. [24]). The remaining parameter values are swept through the range of -2 Hz $<A_{G0}<0$ Hz and 0.2 Hz $<\nu<1.8$ Hz. The range belongs to region III. The black areas indicate the chaos generation while the white ones indicate the attraction by the stable limit cycles. The relation $2/A_L=n+\mu=2\nu$ ($|\mu|<1$) holds in this case, where n is an integer shown in the figure.

reasonable, chaos with a large value of Lyapunov exponent is generated for most values of μ as seen around the region of $A_{G0}=0$ Hz in Fig. 4. This comes from that $|dg(T)/dT|$ becomes larger than unity in the region as shown below. The derivative is represented as

$$\frac{dg(T_0)}{dT_0}=\frac{dT_2}{dT_0}=\frac{dT_2}{dT_1}=\frac{dH_G(\tau_2)}{d\tau_2}\Big/\frac{dH_G(\tau_1)}{d\tau_1} , \quad (3.18)$$

because $dT_1/dT_0=1$ and $d\tau_2/d\tau_1=1$ as seen from Eqs. (3.11) and (3.12). Using Eqs. (2.22) and (2.18), we obtain

$$\frac{dH_G(\tau)}{d\tau}=1+\frac{\Gamma_G}{A_G}\sin(2\pi\tau) . \quad (3.19)$$

We now define τ_C by using the relations $\sin(2\pi\tau_C)=-A_G/\Gamma_G$ and $\Gamma_G\cos(2\pi\tau_C)>0$. We further define τ_D, which is slightly less than τ_C, by using the relation $\cos(2\pi\tau_D)-\cos(2\pi\tau_C)=2\pi A_G/\Gamma_G$. Because τ_1 is the minimum solution τ of the equation $\Theta_G(\tau;T_0)=A_G(\tau-T_0)-(\Gamma_G/2\pi)\cos(2\pi\tau)=-1$, τ_1 must lie between τ_D+k and τ_C+k, where k is some integer. In the case of $|\Gamma_G|\gg -A_G$, the approximation $|\sin(2\pi\tau_D)|=[1-\cos^2(2\pi\tau_D)]^{1/2}\doteq 2|\pi A_G/\Gamma_G|^{1/2}$ is applicable. Then, we obtain $|dH_G(\tau_1)/d\tau_1|\lesssim 2|\pi\Gamma_G/A_G|^{1/2}$ from Eq. (3.19). On the other hand, $|dH_G(\tau_2)/d\tau_2|$ is of the order of $|\Gamma_G/A_G|$ for most values of μ, because $\tau_2=\tau_1+2/A_L$ and $2/A_L=n+\mu$. Therefore, $|dg(T_0)/dT_0|$ becomes of the order of or larger than $|\Gamma_G/A_G|^{1/2}$ for most values of μ.

In the case where $B_G=B_L=0$, $\Gamma_L=0$, and $|\Gamma_G|>-A_G$, chaos occurs usually in the two kinds of parameter regions: (i) $2/A_L$ is slightly smaller than an arbitrary integer and (ii) $|\Gamma_G|\gg -A_G$. The chaos generation arises from the reason that the absolute value of average of $dg(T)/dT$ exceeds unity. In the outside of

these regions the chaos generation is possible but rare, as seen in Fig. 4, where chaos sometimes arises from the orbit localization mechanism described later.

Next we consider the case where $B_G=B_L=0$, $\Gamma_L\neq 0$, and $|\Gamma_G|>-A_G$. When $|\Gamma_L|<A_L$, that is, $f_L(\tau)$ is continuous, Eq. (3.15) holds also in this case for $2/A_L=n$. The parameter dependence of chaos generation derived in the case of $\Gamma_L=0$ is also generally applicable as shown in Fig. 5. When $|\Gamma_L|>A_L$, the chaos generation depends on the signatures of Γ_G and Γ_L. In the case of $\Gamma_L\Gamma_G>0$, the dependence derived for $\Gamma_L=0$ is still usable for the region where $|\Gamma_L|$ is close to A_L, but it becomes inapplicable as $|\Gamma_L|$ increases. Then the investigation on the map g shows that chaos generation is stopped by a tangent bifurcation. In the case of $\Gamma_L\Gamma_G<0$, chaos is generated in the broader region compared with the case of $\Gamma_L\Gamma_G>0$ as shown in Fig. 5. On the hyperplane determined by $\Gamma_G/A_G=\Gamma_L/A_L$ in the parameter space, $g(T)$ becomes a translational map similar to the mapping given by Eq. (3.15). It is seen in Fig. 5 that the phase diagram in the vicinity of the hyperplane has a rather complicated structure with a kind of self-similarity.

Finally we consider the case where $B_G<0$ and $B_L<0$. The consideration made for the case of $B_G=B_L=0$ is almost applicable to the present case. Chaos can be generated by the phase shift in which H_G loses monotonicity and f_L shifts τ_{GL} to τ_{LG} so that the absolute value of average of $dg(T)/dT$ exceeds unity. The conditions for the parameters A_G, A_L, Γ_G, and Γ_L under which chaos occurs usually are similar to those in the case of $B_G=B_L=0$ as seen in Fig. 6. However, in the case of $B_G<0$, Eq. (3.11) does not hold and T_1 becomes a monotonic function of T_0 with a discontinuous point. Although the discontinuous shift is small in the region near $B_G=0$, it broadens as $|B_G|$ increases. Therefore, the Lyapunov exponent of $g(T)$ decreases and the chaos generation region becomes narrower as $|B_G|$ increases. When $|B_G|$ is large enough, chaos becomes extremely rare. In the cases where at least one of B_L and B_G is nonzero, there appears no characteristic complexity in the phase diagram at the vicinity of the hyperplane $\Gamma_G/A_G=\Gamma_L/A_L$ as shown in Fig. 6.

The Lyapunov exponent ($\mathcal{L}$) used in the present paper is calculated by

$$\mathcal{L}\equiv\lim_{n\to\infty}\frac{1}{n}\sum_{m=0}^{n-1}\ln\left\{\left.\frac{df(\tau)}{d\tau}\right|_{\tau=f^m(\tau_0)}\right\}$$
$$=\lim_{n\to\infty}\frac{1}{n}\sum_{m=0}^{n-1}\ln\left\{\left.\frac{dg(T)}{dt}\right|_{T=g^m(T_0)}\right\}, \tag{3.20}$$

where τ_0 and T_0 are the initial values of τ_{GL} and T_G, respectively, and $f^m(\tau_0)$ and $g^m(T_0)$ are the values obtained after m times applications of f and g, respectively.

2. *Orbit localization*

Chaos detected by our numerical calculations in the region of $B_L\leq 0$ and $B_G\leq 0$ are usually caused by the phase shift. However, there exist some chaotic solutions originating from the other mechanisms, although the parameter regions where these types of chaos occur are very narrow. We describe the two unique mechanisms detected so far in the present and following subsections.

It may occur for some parameter values that an invariant set (attractor) of the mapping functions f and/or g consists of a definite number of narrow intervals of variable $(J_1,J_2,\ldots,J_N)$ as shown in Fig. 7 where $N=1$. This means that the chronological sequence (orbit) of τ_{RS} is localized within a definite number of narrow intervals. In order to make clear the chaos generation mechanism, first we consider the feature of discontinuities in the functions $f(\tau)$ and $g(T)$. When $F_S(T_S)$ defined by Eq. (2.31) has a discontinuity at $T_S=T_{S0}$, the values of $F_S(T_S)$ depend linearly on T_S in one hand neighbored region of T_{S0} but change as $|T_S-T_{S0}|^{1/2}$ in the opposite-hand neighbored regions of T_{S0} as shown in Fig. 7. By using the definition $f_S(\tau_{RS})=f_S(T_S)$, and Eqs. (2.28) and (2.32), it is shown that f_S, f, and g have the analogous feature around their discontinuous points. This means that their mapping operation around the discontinuity is linear on the one side and square-root-like on the other side.

Next we consider the case where a finite number of in-

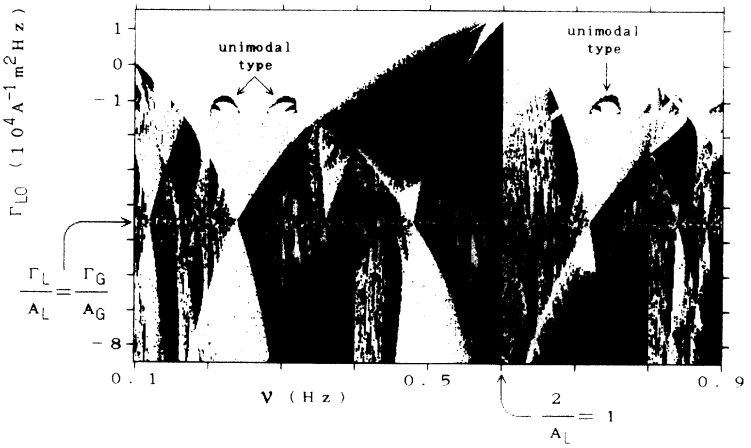

FIG. 5. Phase diagram in the case of $A_{L0}=1.2$ Hz, $A_{G0}=-0.8$ Hz, $B_{L0}=0$ Hz, $B_{G0}=0$ Hz, $\Gamma_{G0}=3\times10^4$ Hz A^{-1}m^2, and $J_0=1\times10^{-4}$ A m^{-2}. The remaining parameter values are swept through the range of -8.5×10^4 Hz A^{-1}m^2 $<\Gamma_{L0}<1.5\times10^4$ Hz A^{-1}m^2 and 0.1 Hz $<\nu<$ 0.9 Hz. The range belongs to region III. The black areas indicate the chaos generation while the white ones indicate the attraction by the stable limit cycles. The relation $2/A_L=1+\mu=5\nu/3$ holds in this case. The diagram has a complicated structure with a kind of self-similarity in the vicinity of the horizontal line given by $\Gamma_L/A_L=\Gamma_G/A_G$.

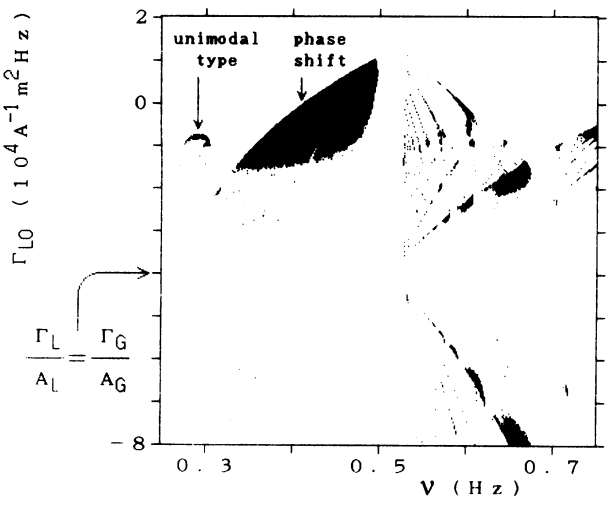

FIG. 6. Phase diagram in the case of $A_{L0}=1$ Hz, $A_{G0}=-1$ Hz, $B_{L0}=-0.05$ Hz, $B_{G0}=-0.05$ Hz, $\Gamma_{G0}=4\times10^4$ Hz A^{-1} m^2, and $J_0=1\times10^{-4}$ A m^{-2}. The remaining parameter values are swept through the range of -8×10^4 Hz A^{-1} $m^2<\Gamma_{L0}<2\times10^4$ Hz A^{-1} m^2 and 0.25 Hz $<\nu<$ 0.75 Hz. The range belongs to region III. The black areas indicate the chaos generation, while the white ones indicate the attraction by the stable limit cycles. The diagram has no particular complexity in the vicinity of the horizontal line given by $\Gamma_L/A_L=\Gamma_G/A_G$.

tervals $(J_1,J_2,\ldots,J_n)$ are mapped into themselves by an operation of g. If g is discontinuous at $T=T_D$, the derivative of g becomes proportional to $|T-T_D|^{-1/2}$ around T_D on one side as shown in Fig. 7. When at least one component J_n of the invariant set contains this quite steep gradient, chaos can be generated from the large slope of g around the discontinuous point that is usually an inner point of J_n. In the case of Fig. 7 the steep slope

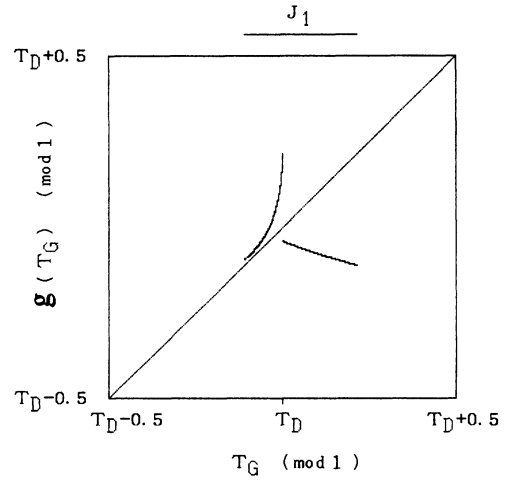

FIG. 7. Chaotic attractor of g in the case of $A_{L0}=1.91$ Hz, $A_{G0}=-0.09$ Hz, $B_{L0}=0$ Hz, $B_{G0}=0$ Hz, $\Gamma_{L0}=1\times10^4$ Hz A^{-1} m^2, $\Gamma_{G0}=1\times10^4$ Hz A^{-1} m^2, $J_0=0.2\times10^{-4}$ A m^{-2}, and $\nu=0.59$ Hz. The values of T_G and $g(T_G)$ are plotted in modulus 1. Chaos is generated by the orbit localization and the attractor consists of a single interval J_1 that contains the discontinuous point T_D in its interior. The derivative of g becomes very large at the left side of T_D.

appears on the left side of the discontinuity. It seems difficult, unlike the cases of the phase shift, for us to give a simple description of the parameter regions where chaos tends to occur by the present mechanism, the orbit localization.

3. *Unimodal type*

When chaos is generated by the mapping function f whose graph is smooth and unimodal like the graph of logistic maps, we refer to the generation mechanism as the unimodal type. We show one example of such a function f in Fig. 8. The function f becomes smooth and unimodal only in some confined interval and the sequence of τ_{GL}'s is confined within the interval. We can see the period-doubling cascades in the neighborhood of the chaos region as in the case of the logistic maps.

The unimodal type has been detected when the relations $|\Gamma_S|\gg|A_S|$, $|\Gamma_R|<|\mp A_R+B_R|$, and $\Gamma_S\Gamma_R<0$ are satisfied, where $R=G$ for $S=L$ and $R=L$ for $S=G$. A typical example for $S=G$ and $R=L$ is shown in Fig. 5 where $A_G=-0.8$ Hz/ν, $B_G=0$, $\Gamma_G=3$ Hz/ν, $A_L=1.2$ Hz/ν, $B_L=0$, and $\Gamma_L=[3\times10^{-4}$ A m^{-2} Hz$]$ Γ_{L0}/ν. The values of $|\Gamma_R|$ seem to be limited in a very narrow range close to $|\mp A_R+B_R|$ as seen in Fig. 5, in which f is smooth but has a large slope within the confines of the interval. It is shown in Fig. 5 that the unimodal type of chaos appears in pairs of small areas of the phase diagram by the side of the phase-shift areas. This type of chaotic orbits can be obtained also for negative values of B_L and/or B_G as seen in Fig. 6 unless their absolute values are very large, although it becomes rare as $|B_S|$s increase.

We have not yet searched exhaustively the parameter space in order to obtain not only the two unique types of chaos mentioned above, but also any other unique types of chaos.

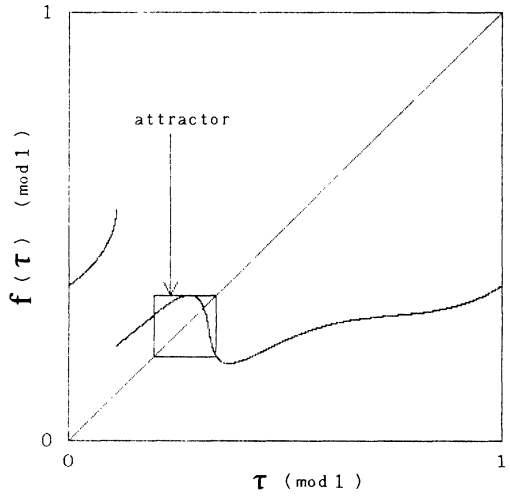

FIG. 8. Graphic representation of the mapping function f in the case of $A_{L0}=1.2$ Hz, $A_{G0}=-0.8$ Hz, $B_{L0}=0$ Hz, $B_{G0}=0$ Hz, $\Gamma_{L0}=-1\times10^4$ Hz A^{-1} m^2, $\Gamma_{G0}=1\times10^4$ Hz A^{-1} m^2, $J_0=3\times10^{-4}$ A m^{-2}, and $\nu=0.22$ Hz. The function f is smooth and unimodal on the attractor, which is indicated by the framework.

4. *Chaos in the region where $B_G > 0$ and/or $B_L > 0$*

We have described so far the chaotic solutions in the parameter region where both B_L and B_G are nonpositive, because it is the case in the membrane systems. However, there may be some other physical systems whose property is described by Eq. (2.8) for $B_G > 0$ and/or $B_L > 0$. Therefore, we would like to describe briefly the chaos generation mechanisms in the case of $B_G > 0$ and/or $B_L > 0$. We refer to those mechanisms as "the acceleration" in the lump, because the term $B_S\Theta$ in Eq. (2.8) accelerates the change of Θ when B_S is positive.

There exists a tendency that the chaos generation area increases in region III as B_S increases. In order to verify the tendency, we consider the dependence of the derivative of the partial mapping function f_S on B_S. The derivative is represented as

$$\frac{df_S(\tau_{RS})}{d\tau_{RS}} = \frac{dT_S}{d\tau_{RS}} \Big/ \frac{dT_S}{d\tau_{SR}} , \tag{3.21}$$

where $T_S = H_S(\tau_{RS})$ and $\tau_{SR} = f_S(\tau_{RS})$. Using Eq. (2.23), we derive

$$\frac{dT_S}{d\tau_{RS}} = 1 + \frac{2\pi G_S \sin(2\pi\tau_{RS} + \delta_S)}{A_S + B_S[G_S\cos(2\pi\tau_{RS} + \delta_S) \mp 1]} . \tag{3.22}$$

The relation between T_S and τ_{SR} is obtained from Eq. (3.10) for $\tau = \tau_{SR}$ as

$$T_S = \tau_{SR} - \frac{1}{B_S}\ln\left[1 + \frac{B_S}{A_S}\{G_S\cos(2\pi\tau_{SR} + \delta_S) \pm 1\}\right] . \tag{3.23}$$

Thus we obtain

$$\frac{dT_S}{d\tau_{SR}} = 1 + \frac{2\pi G_S \sin(2\pi\tau_{SR} + \delta_S)}{A_S + B_S[G_S\cos(2\pi\tau_{SR} + \delta_S) \pm 1]} . \tag{3.24}$$

When $|G_S| < 1$, the absolute value of the denominator in Eq. (3.22) becomes smaller as B_S increases, but that in Eq. (3.24) becomes larger as B_S increases. The second term on the right-hand side of Eq. (3.22) becomes dominant depending on the value of τ_{RS} in region III. When f_S has discontinuities, that is, $A_L + B_L - |\Gamma_L| < 0$ for $S = L$ or $A_G - B_G + |\Gamma_G| > 0$ for $S = G$, the second term on the right-hand side of Eq. (3.24) also becomes dominant. Thus the slope of f_S given by Eq. (3.21) often becomes steeper as B_S increases within such regions. The same tendency can be observed even in the region of $|G_S| \geq 1$. Because the Lyapunov exponent of the system may increase with B_S, the tendency to generate chaos is enhanced with increasing B_S. It is seen in Fig. 9 that the chaotic sequences of τ_{RS} are obtained in a broader area of region III as B_Ss increase.

When B_S is positive and fixed, the Lyapunov exponent in the case of $B_R < 0$ tends to becomes smaller compared with that for $B_R > 0$. When $B_R < 0$, the area where chaos is generated decreases with increasing $|B_R|$.

The signs of Γ_G and Γ_L also affect the tendency to the chaos generation. In the case of $\Gamma_G\Gamma_L < 0$, the numerical calculation shows that chaos covers most the part of the parameter region where both of f_G and f_L have discontinuities, that is, $|\Gamma_G| > -A_G + B_G$ and $|\Gamma_L| > -A_L + B_L$. This is because $dg(T)/dT$ becomes larger than unity for most values of T in the region. On the other hand, when $\Gamma_G\Gamma_L > 0$ and B_G and B_L are sufficiently small, chaos is rather rare in the region where both f_G and f_L are discontinuous. This comes from that $|dg(T)/dT|$ becomes less than unity for most values of T in such cases. However, in the parameter region where both f_L and f_G are continuous, the distribution of the chaos generation area scarcely depends on the signs of Γ_G and Γ_L.

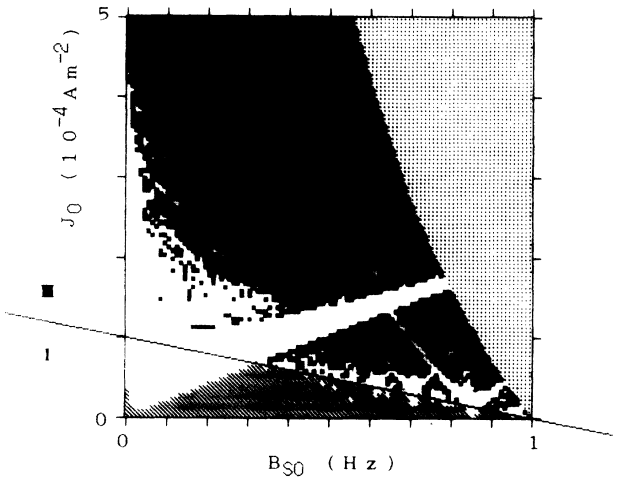

FIG. 9. Phase diagram in the case of $A_{L0} = 1$ Hz, $A_{G0} = -1$ Hz, $\Gamma_{L0} = 1\times10^4$ Hz A^{-1} m^2, $\Gamma_{G0} = -1\times10^4$ Hz A^{-1} m^2, and $\nu = 1$ Hz. The remaining parameter values are swept through the range of $B_{L0} = B_{G0}$, 0 Hz $< B_{L0} <$ 1 Hz, and 0 A m^{-2} $< J_0 < 5\times10^{-4}$ A m^{-2}. The black, white, and hatched areas indicate the chaos generation, the attraction by the stable limit cycles, and the quasiperiodicity, respectively. Because the parameter values do not satisfy Eqs. (2.25)–(2.27) in the dotted area, the continuous oscillation of Θ does not occur there. Regions I and III are indicated. The chaos area increases as B_{sS} increase.

C. Stable chaos

The present system contains the stable chaotic attractors which are never destroyed under any slight changes in the parameter values as seen in Figs. 4–6 and 11. The reason why the structurally stable chaos occurs in the system is as follows. When chaos is generated by the phase-shift mechanism, the derivative of $g(T)$ usually becomes positive (or negative) at every T. Thus the absolute value of $dg(T)/dT$ becomes uniformly larger than a certain positive number ϵ, where ϵ exceeds unity in some pats of the parameter regions. In such parts, the Lyapunov exponent of g clearly exceeds unity and the sequence of T becomes chaotic. Because the condition that the inequality $|dg(T)/dT| > \epsilon$ holds for any values of T cannot be broken by any slight variations of the parameter values, the chaos becomes structurally stable.

The same statement may also hold even if $\epsilon \leq 1$. In the case of $0 < \epsilon \leq 1$, the sequence of T may settle in a stable limit cycle or a chaotic attractor depending on the parameter values and the initial condition. When g has a chaotic attractor with the positive Lyapunov exponent and the inequality $|dg(T)/dT| > \epsilon$ holds uniformly on the attractor region, it is highly possible on the basis of the numerical verification for various relevant cases that $|dg^N(T)/dT|$ exceeds unity uniformly on the attractor for a sufficiently large value of N, where g^N means the mapping function made by the N times iterative operation of g. The chaos also becomes structurally stable in such cases. If the minimum value of N satisfying the inequality is relatively small, the stable chaos occurs usually over a large area in the parameter space without any windows of nonchaotic solution. On the other hand, when the minimum value of N is not small, the very narrow areas (windows) in which the stable periodic orbits appear through tangent bifurcations are sometimes inserted in the chaos area. However, the interweavement of the windows is not dense in the parameter space unlike the logistic maps and the sine circle maps. There exists no periodic-doubling cascade within these windows either.

In the present system, the structurally stable chaos arises from the characteristic feature that the mapping function $f(\tau)$ or $g(T)$ may have discontinuities. In general, the stable chaos is possible also in continuous one-dimensional discrete systems. For example, a smooth circle map p such that $p(x+n)=p(x)+n$ for every x may generate the structurally stable chaos if $|n| > 1$. When $|n| \leq 1$, the stable chaos may be generated if the mapping function has nondifferentiable points within the chaotic attractor, such as the tent map or the one-dimensional return map of the Lorentz system. The stable chaos can be generated also in smooth dynamical systems of higher dimensions, as seen in the Ruelle-Takens picture [30] for the route to chaos, in which a perturbation destroys the motion on a 3-torus and induces the transition to chaos.

Because f or g is piecewise smooth, the derivative of f or g can be obtained at each point through approaching at least from either its right or left side. We now refer to the point as "the critical point" at which the derivative of the function obtained by approaching to the point at least from one side becomes zero. If f or g has a chaotic attractor which contains no critical points, the chaos is probably structurally stable for the aforementioned reason. When the chaotic attractor contains one or more critical points, the chaos is probably structurally unstable because of the reason described in Sec. IV A. If the mapping function is smooth everywhere on the chaotic attractor, the attractor contains probably at least one critical point for the reason described in Sec. IV A too.

In the case where $B_G \leq 0$ and $B_L \leq 0$, the chaotic attractors are generated usually through the phase shift or the orbital localization and most of them have no critical points. If the chaotic attractor is of the unimodal type, it contains one critical point. In the case where $B_G \geq 0$ and/or $B_L \geq 0$, the appearance of chaotic attractors which contain no critical points becomes less frequent as B_G and/or B_L increase, although the chaos generation as a whole becomes more frequent. This comes from the fact that it becomes more difficult as B_G and/or B_L increase that the value of $dg(T)/dT$ does not vanish over the whole attractor range.

D. Routes to chaos

First we summarize briefly the routes to chaos [31] which exist in the present system on the basis of the calculated results in the preceding subsections. Second we describe in detail the bifurcation that appears under the variation of the amplitude J_0 and/or frequency ν of the applied current in the two regions where chaotic attractors may be generated by the two main mechanisms, the phase shift and the acceleration.

The types of route to chaos confirmed in the present system are (i) period-doubling cascades [32–36], which occur in the case of unimodal type f or the case where the values of B_L and/or B_G are positive, but we have not yet detected the cascades in the region where $B_S \leq 0$ and $\Gamma_S > 0$ for $S = L$ and G; (ii) intermittency [37,38], which occurs independently of the sign of B_S, because the intermittency appears just before a tangent bifurcation occurs [37] and the disappearance of chaos due to the tangent bifurcation takes place in the present system independently of the sign of B_S; (iii) the U sequence [39,40], which occurs in the case of unimodal type f or in the regions where the values of B_L and/or B_G are positive, because the U sequence is a universal feature of the unimodal mapping functions; (iv) the quasiperiodic-chaotic transition [41–43], closely related to the sine circle maps, which occurs in the region of $B_L > 0$ and/or $B_G > 0$ as shown below (the periodic-quasiperiodic-chaotic sequence suggested by Ruelle and Takens [44] cannot occur because the Ruelle-Takens picture is applicable only for the system whose Poincaré section has at least two dimensions); and (v) the transition from quasiperiodicity to chaos via complete phase locking, which occurs in the region where chaos is generated by the phase shift as shown below.

1. *The region of $B_S < 0$ and $\Gamma_S > 0$ ($S = L$ and G)*

As J_0 is increased, the system passes from region I to region III via region II in which the complete phase locking may occur, that is, the measure of quasiperiodicity may vanish as shown in Fig. 10. The figure shows the typical route to chaos in the case of $B_S < 0$ and $\Gamma_S > 0$ ($S = L$ and G). When we increase J_0 along the line of $\nu = 0.75$ Hz in Fig. 10, the dynamic state of the system is changed as the following sequence: (i) mostly quasiperiodic for $0\ \mathrm{A\,m^{-2}} \leq J_0 \leq 0.32 \times 10^{-4}\ \mathrm{A\,m^{-2}}$; (ii) complete phase locking for $0.32 \times 10^{-4}\ \mathrm{A\,m^{-2}} < J_0 \lesssim 0.775 \times 10^{-4}\ \mathrm{A\,m^{-2}}$ where g is monotonic but a gap exits in the functional values of $g(T)$; (iii) mostly chaotic for $0.775 \times 10^{-4}\ \mathrm{A\,m^{-2}} \lesssim J_0 \lesssim 1.24 \times 10^{-4}\ \mathrm{A\,m^{-2}}$ where the values of $g(T)$ overlap double and the derivative of $g(T)$ is positive everywhere; and (iv) periodic for $J_0 \gtrsim 1.24 \times 10^{-4}\ \mathrm{A\,m^{-2}}$, where a tangent bifurcation takes place at $J_0 \doteq 1.24 \times 10^{-4}\ \mathrm{A\,m^{-2}}$.

The transition from the quasiperiodicity to the chaos via the frequency locking can be observed also in the sine

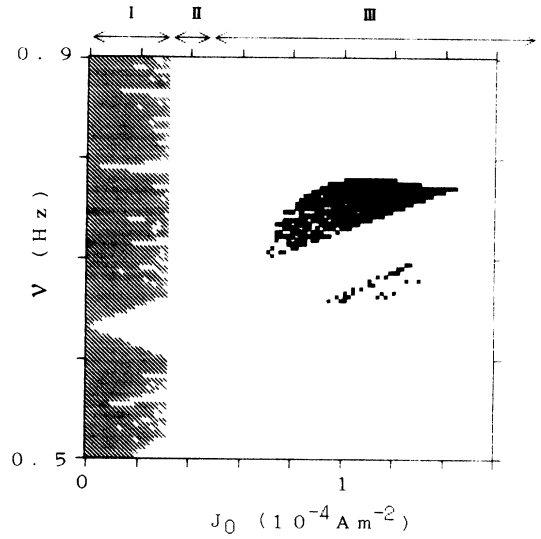

FIG. 10. Phase diagram in the case of $A_{L0}=1.6$ Hz, $A_{G0}=-0.4$ Hz, $B_{L0}=-0.32$ Hz, $B_{G0}=-0.08$ Hz, $\Gamma_{L0}=1\times10^4$ Hz A^{-1} m^2, and $\Gamma_{G0}=1\times10^4$ Hz A^{-1} m^2. The remaining parameter values are swept through the range of 0 A m^{-2} $<J_0<$ 1.6×10^{-4} A m^{-2} and 0.5 Hz $<\nu<$ 0.9 Hz. The black, white, and hatched areas indicate the chaos generation, the attraction by the stable limit cycles, and the quasiperiodicity, respectively. Regions I, II, and III are indicated. Region II separates the quasiperiodicity area from the chaos generating area.

circle maps, as the nonlinearity is gradually increased. The complete phase locking is restricted to the transition line in the parameter space beyond which the map loses monotonicity. However, in the present system, the complete phase locking occurs over a finite width, region II, in the parameter space, so that the quasiperiodicity is separated from the chaos by a finite distance in the phase diagram as seen in Fig. 10. The transition from the quasiperodicity to the chaos via the complete phase locking does not occur in the integrate-and-fire model [25] and the simple drive-relaxation-oscillator model [26] but does in the modulated-relaxation-oscillator models [27,28].

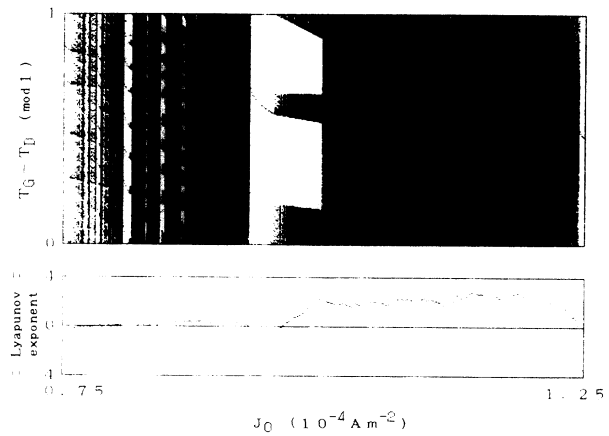

FIG. 11. Attractor bifurcation diagram obtained by increasing J_0 from 0.75×10^{-4} to 1.25×10^{-4} A m^{-2} along the line of $\nu=0.75$ Hz in Fig. 10. The distribution of T_G-T_D in modulus 1 on the attractor (above) and the Lyapunov exponent (below) are plotted against the value of J_0. The first 500 iterations have been discarded to avoid the transients and the subsequent 5000 iterations are used. The Lyapunov exponent becomes negative when the chronological sequence of T_G is attracted by a stable limit cycle. There exist the chaotic attractors which cover only a few narrow intervals of T_G, although most of the chaotic attractors cover the whole range of T_G in modulus 1.

We show a diagram of attractor bifurcation due to the variation of J_0 in Fig. 11. Most of the region of 0.775×10^{-4} A m^{-2} $\lesssim J_0 \lesssim$ 1.24×10^{-4} A m^{-2} is covered with the stable chaos as seen from the graph of Lyapunov exponent in Fig. 11, even though the chaos is interwoven with the windows of stable periodic state through the tangent bifurcation. There exist the chaotic attractors which cover only a few narrow intervals of T_G as seen in Fig. 11, although most of the chaotic attractors cover the whole range of T_G in modulus 1. We explain in detail how the chaotic attractors are divided into a definite number of subbands in Appendix B.

2. *The region of $B_S>0$ ($S=L$ and G)*

When J_0 is increased, the system passes directly from region I, in which the quasiperiodic sequences of τ_{RS} are observed frequently, to region III, in which chaos can be observed. This is because as J_0 is increased, the function f loses monotonicity earlier than it loses continuity as seen from Eqs. (3.1) and (3.2)–(3.5). Since f is smooth at the boundary between these two regions, the routes to chaos belong to the same types as those which have been found in the sine circle maps [45]. Therefore, we can see the period-doubling cascades, the U sequence, etc. also in the present system. However, when we increase J_0 further, f loses continuity besides monotonicity, unlike in the sine circle maps. In such reigns, the stable chaos can be generated when the attractor does not contain any critical point of the mapping function f.

IV. DISCUSSION

A. Instability of the chaos in smooth one-dimensional discrete systems

If h is a one-dimensional real function that satisfies $h(x+1)=h(x)+m$ for each x where $m=0$ or 1, like the logistic map or the sine circle map, and the iteration of h generates chaos, the chaotic attractor may be structurally unstable for the following reason. In general, chaotic attractors generated by one-dimensional smooth functions usually have inner points, i.e., their fractal dimension is one. If h has a chaotic attractor C containing inner points, it can be proved that C is composed of a finite number of closed intervals and that h is nonmonotonic within at least one of those intervals. Because h is smooth, there exists at least one point x_C in C at which the derivative of h vanishes, that is, h has a critical point in C. If the chaotic attractor C contains a critical point x_C, the chaotic orbits within C should pass near x_C repeatedly because of the recursiveness of chaotic orbits. Thus it is highly possible that x_C can become a periodic

point by an arbitrarily small perturbation. In the case where x_C is periodic, the orbit containing this point is superstable because of the chain rule of differentiation. Therefore, the attractor C may be replaced by a stable periodic orbit due to an arbitrarily small perturbation, that is, the chaos will be densely interwoven with the windows of stable periodic orbits in the bifurcation phase diagram.

On the other hand, the stable chaos in the one-dimensional discrete dynamical system becomes possible if the mapping function contains at least one discontinuous or nondifferential point such as the function f, because the chaotic attractors need not contain any critical points. The stable chaos has been observed also in an autonomous electric circuit system, where the one-dimensional mapping function is piecewise smooth and has no critical point.

B. Relation of the RPTH model to the integrate-and-fire model

The RPTH model described by Eqs. (2.8) and (2.9) becomes equivalent in the special cases to the integrate-and-fire model studied by Keener, Hoppensteadt, and Rinzel [25]. The time course of the RPTH system is described by the iterative application of the mapping function f, which consists of the alternate mappings of two firing functions f_L and f_G. In the special cases where the equation $f_L(\tau)=f_G(\tau)\text{mod}1$ or $f_L(\tau)=\tau \text{ mod}1$ holds for each τ, the iteration of f virtually produces the same sequence of τ as only that of f_G. Then, transforming the time τ, the variable Θ and the system parameters A_G, B_G, Γ_G in Eqs. (2.8) and (2.9) as

$$t=2\pi(\tau-\tfrac{1}{4}) , \tag{4.1}$$

$$u=\tfrac{1}{2}(1-\Theta) , \tag{4.2}$$

$$\sigma=-\frac{1}{2\pi}B_G , \tag{4.3}$$

$$S=-\frac{1}{4\pi}(A_G+B_G) , \tag{4.4}$$

$$B=\frac{\Gamma_G}{A_G+B_G} , \tag{4.5}$$

we can see that the RPTH model is equivalent to the integrate-and-fire model

$$\frac{du}{dt}=-\sigma u+S\{1+B\cos(t)\} , \tag{4.6}$$

$$u(t+0)=0 \quad \text{if } u(t)=1 . \tag{4.7}$$

By using the functions f in the special case of $f_L(\tau)=\tau$, we consider the dynamical properties of the integrate-and-fire model. It can be verified that the orbit of τ_{LG} is confined in a certain interval K in modulus 1 and the use of g is always reasonable if K contains τ_{LG}. Therefore, we can use g in this special case with no exception. The dynamical properties of the sequence of T_G generated by g are represented in the space of the parameters A_G, B_G, and Γ_G as follows. (i) For the case of $B_G<0$, the quasiperodicity is observed for a parameter set of positive measures in region I where $|\Gamma_G|\leq -A_G+B_G$. The complete phase locking occurs in regions II and III where $|\Gamma_G|>-A_G+B_G$, because f_G is discontinuous and monotonic within K mod1 even in region III. This system generates no chaos. (ii) For the case of $B_G=0$, because the equation $g(T_G)=T_G-2/A_G$ holds for each T_G, the sequence of T_G becomes quasiperiodic for the irrational values of A_G, while it becomes periodic for the rational values of A_G. The orbit is neutrally stable in the latter case. (iii) For the case of $B_G>0$, the quasiperiodicity is often observed in region I where $|\Gamma_G|\leq -A_G-B_G$, while chaos becomes possible in the complementary region III. Chaos covers a major portion of the parameter region given by the inequality $|\Gamma_G|>-A_G+B_G$, in which f_G becomes discontinuous.

The integrate-and-fire model could not generate any chaos in the case of positive damping ($B_G<0$) suitable for the usual physical systems. However, by applying the present system to the problem, we can obtain a simply extended version of the integrate-and-fire model which may generate chaos even for the positive damping. When the partial mapping function f_L is given by

$$f_L(\tau)=\tau+\text{const} , \tag{4.8}$$

chaos may appear in the present system as seen from the consideration about the chaos produced by the phase shift in Sec. III B 1. By representing this situation in terms of the integrate-and-fire model, we obtain the extended version where only Eq. (4.7) is replaced by

$$u(t+t_0)=0 \quad \text{if } u(t)=1 . \tag{4.9}$$

Here t_0 is the fourth parameter of positive value and means a finite resetting time.

C. Relation of the RPTH model to the modulated relaxation oscillator models

Christiansen and co-workers [27,28] have presented the two models in the integrate-and-fire scheme, which are the relaxation oscillators with modulated firing thresholds and generate the complete phase locking (CPL) and chaos. In one of the models [27], the resetting time is zero as the conventional integrate-and-fire model but periodic modulation is introduced on the upper and lower thresholds. In the other model [28], even after the system variable reaches an upper threshold, the variable decreases with a finite relaxation time until a lower threshold is reached. The upper threshold is modulated periodically whereas the lower one is kept constant.

The RPTH model is physically more similar to the model [28] with a finite resetting time than to the model [27] with abrupt resetting, because the RPTH model also has the resetting dynamics. One of the main differences between the model with a finite resetting time and the RPTH model is that the modulation, which induces various nonlinear phenomena, is introduced on a threshold in the former model whereas it is done on the applied current in the latter model.

An interesting point in the modulated relaxation oscil-

lator with a finite resetting time is the coexistence of CPL and chaos in a region of the parameter space. The coexistence occurs also in region III of the RPTH model. However, there is a following qualitative difference between them. In region III of the RPTH model, the mapping function f is always simultaneously nonmonotonic and discontinuous when $B_S<0$ ($S=L$ and G), that is, the positive damping occurs both for the L and the G states, as seen from Eqs. (3.1) and (3.3)–(3.5). Thus CPL and chaos always coexist in the parameter region for the positive dampings. In the modulated relaxation oscillator model, there exists a region in the parameter space where the map is nonmonotonic but continuous for the positive dampings and the route from quasiperiodicity to chaos appeared in the sine circle maps is observed. In the RPTH model, this route is possible only when B_L and/or B_G is positive (negative damping) as denoted previously.

When a temperature modulation is applied to the present system of two solutions divided by a lipid-bilayer membrane, the values of the threshold θ_{RG} and θ_{RL} for the phase transition are changed with the temperature. Then the RPTH model becomes equivalent to the relaxation oscillator with a finite resetting time whose upper and lower thresholds are simultaneously modulated, in the case where $\Gamma_G=\Gamma_L=0$. The dynamical property of the RPTH model under the temperature modulation will be described in a forthcoming paper.

APPENDIX A

We show here that the electric potential ϕ_m across the membrane, the charge density σ_X of the polar head layer, and the H^+ flux Φ^X_{Hm} are described in a reasonable approximation by analytic functions of the concentration fluctuation θ_X of H^+ and OH^- defined by Eq. (2.1) and the applied current J.

The charge density σ_X is represented as

$$\sigma_X=\frac{-FA_{LM}\xi_X}{1+K_H Y^X_H}\ , \tag{A1}$$

by assuming the Langmuir isotherm for the adsorption of H^+ on the lipid polar heads [24], where Y^X_H is the concentration of H^+ at the outside of lipid-layer surface on the side X, ξ_X is the fraction of acidic lipids on the side X, A_{LM} is the areal density of lipid molecules, and K_H is the association constant in the adsorption process of H^+. We neglect the adsorption of M^+ because K_M is extremely small compared with K_H. The surface concentrations Y^X_H and Y^X_M in the double-layer regions are approximated by those in the thermal equilibrium state [24] as

$$Y^X_H=\frac{\bar{C}^{BX}_H}{C^{X\infty}_M}\{(W_X+C^{X\infty}_M)^{1/2}+W_X^{1/2}\}^2\ , \tag{A2}$$

$$Y^X_M=\{(W_X+C^{X\infty}_M)^{1/2}+W_X^{1/2}\}^2\ , \tag{A3}$$

where $C^{X\infty}_M$ is the fixed concentration of M^+ in the outermost solution to the side X,

$$W_X\equiv\frac{1}{8RT\epsilon_S}\left[\frac{\epsilon_m}{2l}\phi_d\mp\sigma_X\right]^2\ , \tag{A4}$$

R and T have the usual meanings, ϵ_S and ϵ_m are the dielectric constants of the solution and the membrane, respectively, l is the width of a lipid layer, ϕ_d is the potential difference between the right and left surfaces of the membrane as shown in Fig. 1, and the upper sign ($-$) and the lower sign ($+$) are used for $X=R$ and L, respectively. Equations (A2) and (A3) are derived from Eq. (6) in a previous paper [24] by using the following approximations. The concentrations $C^B_\nu(x,t)$ of ion ν in the bulk solution regions are replaced by the averaged concentrations $\bar{C}^{BX}_\nu$, because the spatial fluctuations of $C^B_\nu(x,t)$ is small over the regions. Because $\bar{C}^{BX}_H$ is much smaller than $\bar{C}^{BX}_M$, we consider only the terms up to the linear with respect to $\bar{C}^{BX}_H/\bar{C}^{BX}_M$. Finally $\bar{C}^{BX}_M$ is replaced by $C^{X\infty}_M$, because the relative deviation of $\bar{C}^{BX}_M$ from $C^{X\infty}_M$ is quite small compared with that of $\bar{C}^{BX}_H$ from $C^{X\infty}_H$. Because $\bar{C}^{BX}_{OH}$ in Eq. (2.1) is given by $K_W/\bar{C}^{BX}_H$, where K_W is the ion product of water, it is seen from Eqs. (2.1) and (A1)–(A4) that σ_X, $\bar{C}^{BX}_H$, Y^X_H, and Y^X_M are implicitly represented by using the analytic functions of θ_R and ϕ_d.

The diffusion potential ϕ_d is also determined by θ_R as follows. The flux $\Phi^R_{\nu m}$ of the cation ν ($\nu=H,M$) from the right double layer to the right bulk solution is nearly equal to the rightward flux of cation ν across the membrane because of the flux continuity and is represented as

$$\Phi^R_{\nu m}=D^m_\nu\left\{Z^L_\nu\exp\left[-\frac{e\phi_d}{2k_BT}\right]-Z^R_\nu\exp\left[\frac{e\phi_d}{2k_BT}\right]\right\}\ , \tag{A5}$$

where D^m_ν is the diffusion coefficient of cation ν in the membrane, e and k_B have the usual meanings, and Z^L_ν and Z^R_ν are the concentrations of cation ν at the inside of left and right membrane surfaces, respectively. The inside surface concentration Z^X_ν is represented by using the outside surface concentration Y^X_ν as

$$Z^X_\nu=\kappa^X_\nu Y^X_\nu\ , \tag{A6}$$

where κ^X_ν is the partition coefficient of cation ν between the lipid layer and the aqueous solution on the side X. The value of κ^X_ν is dependent definitively on the state of the lipid layer. Substituting Eq. (A5) into Eq. (2.6), we obtain

$$\exp\left[\frac{e\phi_d}{2k_BT}\right]=\left\{\left[\left[\frac{J}{2F}\right]^2+(D^m_HZ^L_H+D^m_MZ^L_M)\times(D^m_HZ^R_H+D^m_MZ^R_M)\right]^{1/2}-\frac{J}{2F}\right\}\Big/(D^m_HZ^R_H+D^m_MZ^R_M)\ . \tag{A7}$$

Thus it is seen from Eqs. (A1)–(A7) and (2.1) that ϕ_d and Φ^R_{Hm} are determined implicitly by θ_R and J.

The membrane potential ϕ_m is represented as

$$\phi_m = \phi_d + \phi_S^L - \phi_S^R \ , \tag{A8}$$

as shown in Fig. 1, where ϕ_S^L and ϕ_S^R are the surface potentials at the left and right solution regions, respectively. The surface potentials are produced by the membrane surface charges σ_X and is denoted as

$$\phi_S^X = -\frac{2RT}{F} \ln \left[\left[1 + \frac{W_X}{C_M^{X\infty}} \right]^{1/2} + \left[\frac{W_X}{C_M^{X\infty}} \right]^{1/2} \right] . \tag{A9}$$

Therefore, ϕ_m is also determined by θ_R and J.

APPENDIX B

We describe how the chaotic attractors are divided into a few narrow intervals (subbands) in modulus 1 as shown in Fig. 11. We call this type chaos a subband attractor. We use the following piecewise linear function g_0 for the mapping function g in order to simplify the problem

$$g_0(T+Z;a,b) \equiv a + bT + Z \ , \tag{B1}$$

where T is the variable with $|T| < \frac{1}{2}$, Z is an arbitrary integer, and a and b are the control parameters. In the case where $b > 1$, the range of g_0 overlaps and the iterative operation of g_0 generates chaos. A subband attractor appears when the value of a is close to an irreducible fraction whose denominator n satisfies the condition of $1 < b^n < 2$. Then the attractor consists of n subbands in modulus 1 and the sum of the measures of the subbands is $b^n - 1$. When the inequality $1 < b^{mn} < 2$ holds for m ($m > 1$), each subband can be further split into $(m+1)$ pieces. The similar statement holds also for the iterative operation of g whose derivative is not a constant function. The variations of J^0 and ν in g correspond to those of a and b in g_0. Keener [29] also studied this type of chaotic attractor using the one-dimensional piecewise smooth functions with positive slopes.

[1] M. R. Guevara, L. Glass, and A. Shrier, Science **214**, 1350 (1981).
[2] H. Hayashi, M. Nakao, and K. Hirakawa, Phys. Lett. **88A**, 265 (1982).
[3] H. Hayashi, S. Ishizuka, M. Ohta, and K. Hirakawa, Phys. Lett. **88A**, 435 (1982).
[4] H. Hayashi, S. Ishizuka, and K. Hirakawa, Phys. Lett. **98A**, 474 (1983).
[5] H. Hayashi, S. Ishizuka, and K. Hirakawa, J. Phys. Soc. Jpn. **55**, 3272 (1986).
[6] G. Matsumoto, K. Aihara, M. Ichikawa, and A. Tasaki, J. Theor. Neurobiol. **3**, 1 (1984).
[7] K. Aihara, G. Matsumoto, and M. Ichikawa, Phys. Lett. **111A**, 251 (1985).
[8] G. Matsumoto, K. Aihara, Y. Hanyu, N. Takahashi, S. Yoshizawa, and J. Nagumo, Phys. Lett. **123A**, 162 (1987).
[9] D. R. Chialvo, R. F. Gilmour, and J. Jalife, Nature **343**, 653 (1990).
[10] J. Rinzel and R. N. Miller, Math. Biosci. **49**, 27 (1980).
[11] K. Aihara, G. Matsumoto, and Y. Ikegaya, J. Theor. Biol. **109**, 249 (1984).
[12] J. H. Jensen, P. L. Christiansen, A. C. Scott, and O. Skovgaard, Physica **13D**, 269 (1984).
[13] T. R. Chay and Y. S. Lee, Biphys. J. **45**, 841 (1984).
[14] C. C. Canavier, J. W. Clark, and J. H. Byrne, Biophys. J. **57**, 1245 (1990).
[15] R. E. Plant, J. Math. Biol. **11**, 15 (1981).
[16] T. R. Chay, Biol. Cybernetics **50**, 301 (1984).
[17] T. R. Chay and J. Rinzel, Biophys. J. **47**, 357 (1985).
[18] T. R. Chay, Physica **16D**, 233 (1985).
[19] R. Blumenthal, J. Theor. Biol. **49**, 219 (1975).
[20] T. R. Chay, J. Theor. Biol. **80**, 83 (1979).
[21] A. Karlin, J. Theor. Biol. **16**, 306 (1967).
[22] H. Kijima and S. Kijima, J. Theor. Biol. **71**, 567 (1978).
[23] N. Fuchikami, S. Sawashima, M. Naito, and T. Kambara, Biophys. Chem. **46**, 249 (1993).
[24] K. Yagisawa, M. Naito, K. Gondaira, and T. Kambara, Biophys. J. **64**, 1461 (1993).
[25] J. P. Keener, F. C. Hoppensteadt, and J. Rinzel, SIAM J. Appl. Math. **41**, 503 (1981).
[26] P. Alstrøm, B. Christiansen, and M. T. Levinsen, Phys. Rev. Lett. **61**, 1679 (1988).
[27] B. Christiansen, P. Alstrøm, and M. T. Levinsen, Phys. Rev. A **42**, 1890 (1990).
[28] B. Christiansen, D.-R. He, S. Habip, M. Bauer, U. Krueger, and W. Martienssen, Phys. Rev. A **45**, 8450 (1992).
[29] J. P. Keener, Trans. Am. Math. Soc. **261**, 589 (1980).
[30] S. Newhouse, D. Ruelle, and F. Takens, Commun. Math. Phys. **64**, 35 (1978).
[31] H. L. Swinney, Physica **7D**, 3 (1983).
[32] A. Arneodo, P. Coullet, C. Tresser, A. Libchaber, J. Mauerer, and D. d'Humieres, Physica **6D**, 385 (1983).
[33] P. Collet and J. P. Eckmann, *Iterated Maps of the Interval as Dynamical Systems* (Birkhauser, Boston, 1980).
[34] O. Lanford, Physica **7D**, 124 (1983).
[35] M. J. Feigenbaum, J. Stat. Phys. **19**, 25 (1978).
[36] M. J. Feigenbaum, Physica **7D**, 16 (1983).
[37] J. E. Hirsch, B. A. Huberman, and D. J. Scalapino, Phys. Rev. A **25**, 519 (1982).
[38] Y. Pomeau and P. Manneville, Commun. Math. Phys. **74**, 189 (1980).
[39] J. Guckenheimer, Invent. Math. **39**, 165 (1977).
[40] N. Metropolis, M. L. Stein, and P. R. Stein, J. Comb. Theory A **15**, 25 (1973).
[41] M. J. Feigenbaum, L. P. Kadanoff, and S. J. Shenker, Physica **5D**, 370 (1982).
[42] S. Shenker, Physica **7D**, 301 (1983), Abstract.
[43] S. J. Shenker, Physica **5D**, 405 (1982).
[44] D. Ruelle and F. Takens, Commun. Math. Phys. **20**, 167 (1971).
[45] D. Rand, S. Ostlund, J. Sethna, and E. Siggia, Phys. Rev. Lett. **49**, 132 (1982).

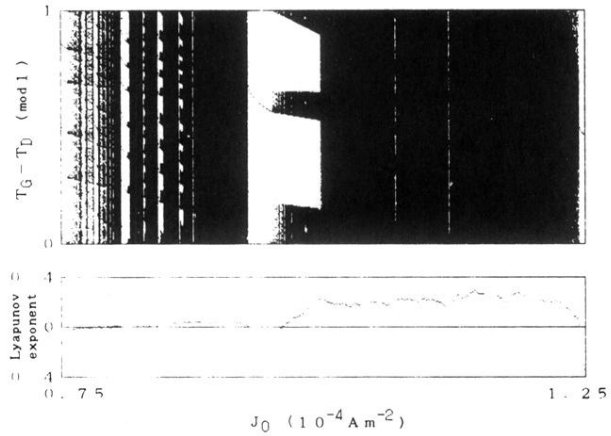

FIG. 11. Attractor bifurcation diagram obtained by increasing J_0 from 0.75×10^{-4} to 1.25×10^{-4} A m^{-2} along the line of $\nu=0.75$ Hz in Fig. 10. The distribution of T_G-T_D in modulus 1 on the attractor (above) and the Lyapunov exponent (below) are plotted against the value of J_0. The first 500 iterations have been discarded to avoid the transients and the subsequent 5000 iterations are used. The Lyapunov exponent becomes negative when the chronological sequence of T_G is attracted by a stable limit cycle. There exist the chaotic attractors which cover only a few narrow intervals of T_G, although most of the chaotic attractors cover the whole range of T_G in modulus 1.

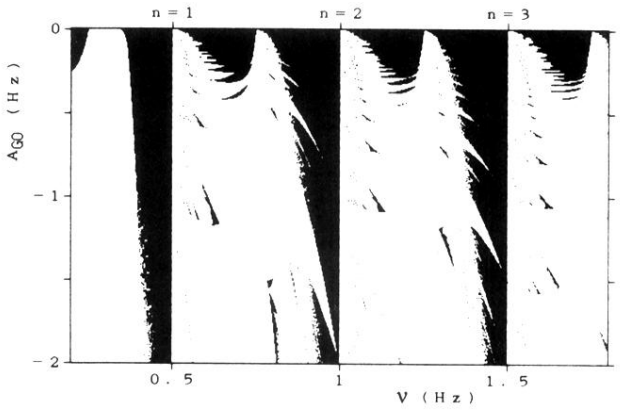

FIG. 4. Phase diagram for the dynamical property of the RPTH system in the case of $A_{L0}=1$ Hz, $B_{L0}=0$ Hz, $B_{G0}=0$ Hz, $\Gamma_{L0}=0$ Hz $A^{-1} m^2$, $\Gamma_{G0}=3\times10^4$ Hz $A^{-1} m^2$, and $J_0=1\times10^{-4}$ $A m^{-2}$ (see Ref. [24]). The remaining parameter values are swept through the range of -2 Hz $< A_{G0} < 0$ Hz and 0.2 Hz $< \nu < 1.8$ Hz. The range belongs to region III. The black areas indicate the chaos generation while the white ones indicate the attraction by the stable limit cycles. The relation $2/A_L = n + \mu = 2\nu$ ($|\mu| < 1$) holds in this case, where n is an integer shown in the figure.

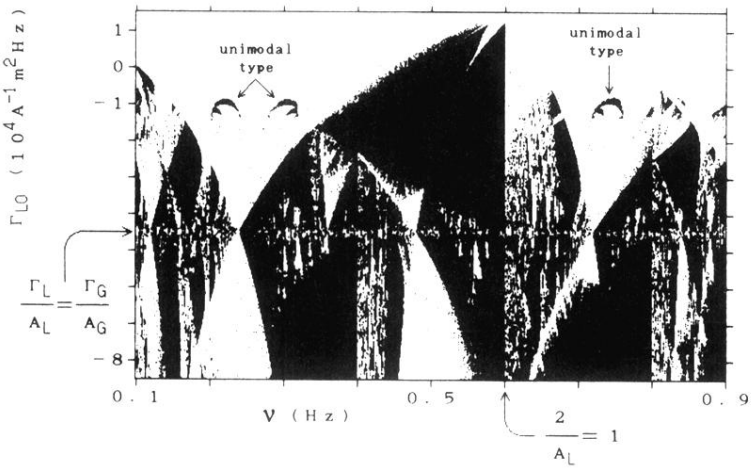

FIG. 5. Phase diagram in the case of $A_{L0}=1.2$ Hz, $A_{G0}=-0.8$ Hz, $B_{L0}=0$ Hz, $B_{G0}=0$ Hz, $\Gamma_{G0}=3\times10^4$ Hz A^{-1}m^2, and $J_0=1\times10^{-4}$ A m^{-2}. The remaining parameter values are swept through the range of -8.5×10^4 Hz A^{-1}m^2 $<\Gamma_{L0}<1.5\times10^4$ Hz A^{-1}m^2 and 0.1 Hz $<\nu<0.9$ Hz. The range belongs to region III. The black areas indicate the chaos generation while the white ones indicate the attraction by the stable limit cycles. The relation $2/A_L=1+\mu=5\nu/3$ holds in this case. The diagram has a complicated structure with a kind of self-similarity in the vicinity of the horizontal line given by $\Gamma_L/A_L=\Gamma_G/A_G$.

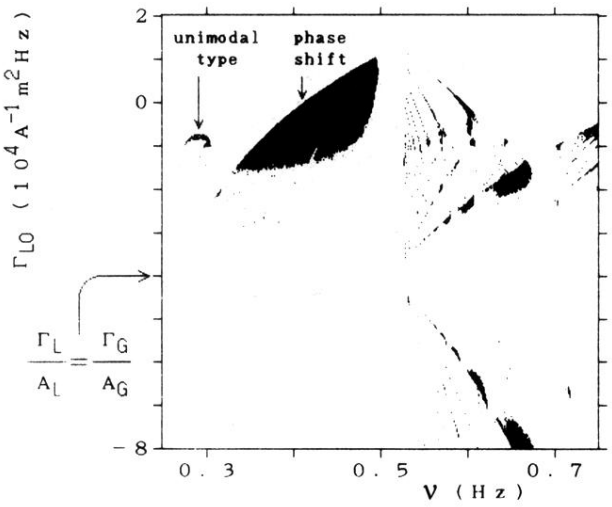

FIG. 6. Phase diagram in the case of $A_{L0}=1$ Hz, $A_{G0}=-1$ Hz, $B_{L0}=-0.05$ Hz, $B_{G0}=-0.05$ Hz, $\Gamma_{G0}=4\times10^4$ Hz A^{-1} m^2, and $J_0=1\times10^{-4}$ A m^{-2}. The remaining parameter values are swept through the range of -8×10^4 Hz A^{-1} m^2 $<\Gamma_{L0}<2\times10^4$ Hz A^{-1} m^2 and 0.25 Hz $<\nu<0.75$ Hz. The range belongs to region III. The black areas indicate the chaos generation, while the white ones indicate the attraction by the stable limit cycles. The diagram has no particular complexity in the vicinity of the horizontal line given by $\Gamma_L/A_L=\Gamma_G/A_G$.

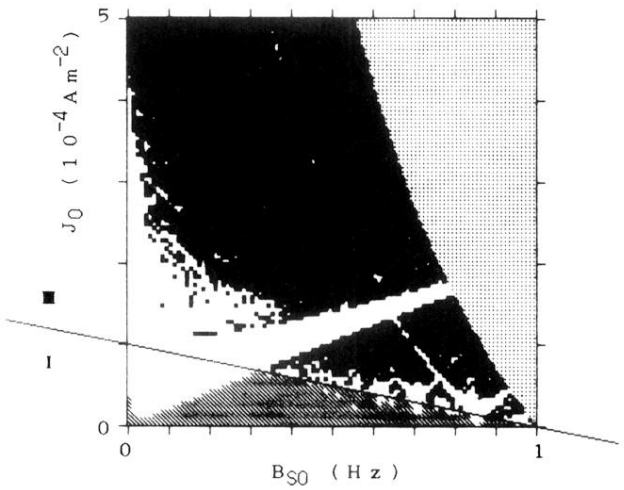

FIG. 9. Phase diagram in the case of $A_{L0}=1$ Hz, $A_{G0}=-1$ Hz, $\Gamma_{L0}=1\times10^4$ Hz A^{-1} m^2, $\Gamma_{G0}=-1\times10^4$ Hz A^{-1} m^2, and $\nu=1$ Hz. The remaining parameter values are swept through the range of $B_{L0}=B_{G0}$, 0 Hz $<B_{L0}<1$ Hz, and 0 A $m^{-2}<J_0<5\times10^{-4}$ A m^{-2}. The black, white, and hatched areas indicate the chaos generation, the attraction by the stable limit cycles, and the quasiperiodicity, respectively. Because the parameter values do not satisfy Eqs. (2.25)–(2.27) in the dotted area, the continuous oscillation of Θ does not occur there. Regions I and III are indicated. The chaos area increases as B_{sS} increase.